



# Quadrotor fault-tolerant incremental nonsingular terminal sliding mode control

Xuerui Wang\*, Erik-Jan van Kampen, Qiping Chu

Delft University of Technology, Kluyverweg 1, 2629HS Delft, the Netherlands

## ARTICLE INFO

### Article history:

Received 16 May 2019

Received in revised form 12 September 2019

Accepted 23 October 2019

Available online xxxx

### Keywords:

Nonsingular terminal sliding mode control

Sensor-based incremental control

Fault-tolerant control

Quadrotor trajectory control

Disturbance rejection

## ABSTRACT

This paper proposes incremental nonsingular terminal sliding mode control for a class of multi-input and multi-output nonlinear systems considering model uncertainties, external disturbances, and sudden actuator faults. This method is free from singularity because it does not involve any negative fractional power. The convergence time in both reaching and sliding phases are proved to be finite. Moreover, by fully exploiting sensor measurements, the proposed incremental control method simultaneously reduces model dependency and the uncertainty remaining in the closed-loop system. The reduction of model dependency simplifies the implementation process and reduces the computational load, while the reduction of uncertainty decreases the minimum possible sliding mode control gains, which is beneficial to chattering reduction. These merits are verified by a quadrotor trajectory tracking problem. Simulation results demonstrate that the proposed method has better robustness against model uncertainties, gusts, and actuator faults than the model-based nonsingular terminal sliding mode control in the literature.

© 2019 Elsevier Masson SAS. All rights reserved.

## 1. Introduction

Autonomous quadrotors have attracted considerable interests from academia and industry by virtue of their mechanical simplicity and capability of hovering, vertically taking off and landing. They are promising platforms for aerial photography, monitoring, package delivery, pesticides spraying, etc. To make full use of the physical benefits of quadrotors, high-precision control laws that can cope with nonlinearities, model uncertainties, gusts, and rotor failures become increasingly important.

Sliding mode control (SMC), as a special type of variable structure control [1,2], is promising in dealing with disturbances and faults. SMC design normally consists of two steps. First, a sliding manifold is designed based on the desired error dynamics. Then, the control input is designed to keep the system trajectories on the sliding manifold. Once the sliding manifold is reached and maintained, the closed-loop system becomes insensitive to model uncertainties and external disturbances [1,2]. Conventionally, linear sliding manifolds are used in SMC because of their simplicity. However, only asymptotic convergence can be achieved by linear sliding manifolds, which means that the time taken for the system trajectories converge to the equilibrium is infinity [1–3]. Terminal

sliding manifolds, which are nonlinear functions of tracking errors, can ensure finite-time convergence in spite of uncertainties and disturbances [4,5].

Control methods that achieve terminal sliding modes are particularly useful for high-precision tracking because they accelerate the convergence near the equilibrium point [4]. A terminal sliding mode control (TSMC) method was proposed for robotic manipulators in [6], but it contains negative fractional powers, which may cause singularities around the equilibrium. A nonsingular TSMC method is proposed in [4] to overcome this issue. The method proposed in [4] uses the discontinuous signum function to ensure the reachability of the manifold, which however leads to the chattering phenomenon. In order to reduce the chattering magnitude, the boundary-layer approximation is adopted in [4]. Nevertheless, this approximation leads to the loss of finite-time convergence, even for a nominal system [7]. In view of this, a continuous TSMC method is proposed in [7]. In the absence of perturbations, this method ensures that the convergence time from any initial condition to the sliding manifold and to the equilibrium are both finite. In the presence of bounded perturbations, this method guarantees finite-time convergence to a small neighborhood of the equilibrium point.

The TSMC method proposed in [7] is concluded to be chattering-free because of its continuous control law. However, it will be shown in this paper that in spite of its continuity, this approach does lead to chattering in some faulty conditions. This paper considers actuator faults, which were not addressed in [4,6,7]. Actuator

\* Corresponding author.

E-mail addresses: X.Wang-6@tudelft.nl (X. Wang), E.vanKampen@tudelft.nl (E.-J. van Kampen), Q.P.Chu@tudelft.nl (Q. Chu).

<https://doi.org/10.1016/j.ast.2019.105514>

1270-9638/© 2019 Elsevier Masson SAS. All rights reserved.

faults are challenging because if the sliding gains are not raised timely after a fault occurs, the resulting uncertainties or perturbations may become unbounded, which further leads to instability of the system. Although amplifying the control gains may help to stabilize the system, it also amplifies the measurement noise and induces chattering. Even under the circumstances that the resulting uncertainties are bounded, to achieve the required performance, the minimum possible sliding control gains are positively correlated to the absolute values of the uncertainties [3,4,7].

A widely used approach to maintain the boundedness of uncertainties and to reduce their absolute values is to identify a physical model of the system online [3]. However, pursuing a perfect model is costly for many complex systems, including aircraft. Online model identification increases the onboard computational load, and the sufficient excitations required by it may also aggravate vibrations [8,9]. These observations lead to a research question: is it possible to simultaneously reduce model dependency and the resulting uncertainty?

The proposal of incremental sliding mode control (INDI-SMC) [10] provides a positive answer to this question. As a hybrid between incremental nonlinear dynamic inversion (INDI) [11] and sliding mode control (SMC), INDI-SMC replaces a part of the model information by sensor measurements, in which way it reduces the remaining uncertainty in spite of its reduced model dependency. Numerical simulations using a nonlinear F-16 aircraft model show that INDI-SMC can achieve desirable tracking performance in the presence of sudden actuator faults and structural damage [10]. However, the boundary-layer approximation used in [10] leads to not only loss of the finite-time reaching phase, but also to robustness impairment. Moreover, Ref. [10] uses linear sliding manifolds, which only achieve asymptotic convergence to the equilibrium point. External disturbances are also not considered in [10]. Recently, an incremental sliding mode control driven by sliding mode disturbance observers approach is proposed in [12] to handle an attitude tracking problem of a quadrotor with one partially impaired rotor. However, this approach also only uses linear sliding manifolds. Although gusts are included in the simulations of [12], the attitudes of a quadrotor are less sensitive to gusts than its trajectories. Considering trajectory control when an actuator fault occurs or when gusts are present is also more meaningful in practice.

This paper proposes an incremental nonsingular terminal sliding mode control (INTSMC) method for second-order nonlinear uncertain systems. Lyapunov analyses show that the proposed method achieves finite-time convergence in both reaching and sliding phases. It is also free from singularity. As compared to the model-based nonsingular terminal sliding mode control (NTSMC) in the literature, the proposed sensor-based approach can simultaneously reduce model dependency and the resulting uncertainty, which consequently decreases the minimum possible sliding mode control gains. When applied to a quadrotor fault-tolerant trajectory tracking problem, simulation results show that the proposed method achieves high-precision control in the presence of model uncertainties, gusts, and successive actuator faults. A wide range of faults can be tolerated without using fault detection and diagnosis or online model identification, which simplifies the design and implementation processes.

The rest of this paper is organized as follows: The INTSMC method will be proposed in Sec. 2. This method will be used to solve a quadrotor fault-tolerant control problem in Sec. 3. The effectiveness of INTSMC will be numerically compared with NTSMC in Sec. 4. Main conclusions are drawn in Sec. 5.

## 2. Incremental nonsingular terminal sliding model control

In this section, the NTSMC derived in [7] for robotic manipulators will first be generalized for a class of nonlinear systems considering model uncertainties, external disturbances and sudden actuator faults in subsection 2.1. The INTSMC will then be proposed based on NTSMC and INDI in subsection 2.2. Theoretical comparisons for the robustness of INTSMC and NTSMC will be presented in subsection 2.3.

Consider a class of multi-input/multi-output nonlinear uncertain systems formulated by:

$$\dot{\mathbf{x}}_1 = \mathbf{G}_1(\mathbf{x}_1)\mathbf{x}_2 \quad (1a)$$

$$\dot{\mathbf{x}}_2 = \mathbf{f}_2(\mathbf{x}_1, \mathbf{x}_2, \kappa(t)) + \mathbf{G}_2(\mathbf{x}_1, \mathbf{x}_2, \kappa(t))\mathbf{u} + \mathbf{d}(t) \quad (1b)$$

$$\mathbf{y} = \mathbf{x}_1 \quad (1c)$$

Define the state vector as  $\mathbf{x} = [\mathbf{x}_1^T, \mathbf{x}_2^T]^T$ , with  $\mathbf{x}_1, \mathbf{x}_2 \in \mathbb{R}^n$ . The input and output vectors are respectively  $\mathbf{u} \in \mathbb{R}^n$  and  $\mathbf{y} \in \mathbb{R}^n$ .  $\mathbf{f}_2$  and the columns of  $\mathbf{G}_1, \mathbf{G}_2$  are smooth vector fields.  $\mathbf{d}(t) \in \mathbb{R}^n$  represents the external disturbance vector.

**Assumption 1.**  $\mathbf{G}_1(\mathbf{x}_1)$  and  $\mathbf{G}_2(\mathbf{x}_1, \mathbf{x}_2, \kappa(t))$  are nonsingular for all  $t$ .

**Assumption 2.** The external disturbance vector  $\mathbf{d}(t)$  is bounded.

In Eq. (1), suppose  $\mathbf{G}_1$  is known for controller design, whereas  $\mathbf{f}_2$  and  $\mathbf{G}_2$  are perturbed by uncertainties and onboard faults, which are modeled as:

$$\begin{aligned} \mathbf{f}_2 &= \bar{\mathbf{f}}_2 + (\mathbf{f}_f - \bar{\mathbf{f}}_2)\kappa(t) + \Phi\theta + \eta_f(\mathbf{x}, t), \\ \mathbf{G}_2 &= \bar{\mathbf{G}}_2 + (\mathbf{G}_f - \bar{\mathbf{G}}_2)\kappa(t) + \Psi\theta + \eta_G(\mathbf{x}, t) \end{aligned} \quad (2)$$

In Eq. (2),  $\bar{\mathbf{f}}_2$  and  $\bar{\mathbf{G}}_2$  are the estimated models used for controller design, while  $\mathbf{f}_f$  and  $\mathbf{G}_f$  denote the post-fault dynamics.  $\kappa(t) \in \mathbb{R}$  is designed as a step function to model the sudden fault at  $t = t_f$  during flight. To be specific,  $t < t_f$ ,  $\kappa = 0$  indicates the fault-free case, and  $t \geq t_f$ ,  $\kappa = 1$  denotes post-fault condition.  $\Phi\theta$  and  $\Psi\theta$  represent parametric uncertainties, where the parameter vector  $\theta \in \mathbb{R}^p$  is not necessarily constant.  $\Phi(\mathbf{x}), \Psi(\mathbf{x}) \in \mathbb{R}^{n \times p}$ , whose columns are smooth vector fields.  $\eta_f, \eta_G \in \mathbb{R}^n$  are smooth vector fields denoting unmodeled dynamics. Under Assumption 1, the uncertainties considered in Eq. (2) satisfy the matching condition [3]. It will be shown in Sec. 3 that both the translational and rotational dynamics of a quadrotor can be modeled by Eqs. (1), (2).

Denote the output reference vector as  $\mathbf{y}_r = \mathbf{x}_{1,r} \in \mathbb{R}^n$ , which should be at least twice differentiable, with bounded  $\dot{\mathbf{y}}_r$  and  $\ddot{\mathbf{y}}_r$ . To stabilize the tracking error  $\mathbf{e} = \mathbf{y} - \mathbf{y}_r$ , NTSMC and INTSMC will be respectively designed in subsections 2.1 and 2.2.

### 2.1. Nonsingular terminal sliding model control

The nonsingular terminal sliding manifold is given by [7]:

$$\mathbf{s} = \mathbf{e} + \Lambda \text{sig}(\dot{\mathbf{e}})^\gamma = \mathbf{0} \quad (3)$$

where  $\text{sig}(\dot{\mathbf{e}})^\gamma = [|e_1|^{\gamma_1} \text{sign}(e_1), \dots, |e_n|^{\gamma_n} \text{sign}(e_n)]^T$ ,  $\Lambda = \text{diag}([\lambda_1, \dots, \lambda_n]^T)$ ,  $\gamma = [\gamma_1, \dots, \gamma_n]^T$ , and  $\lambda_i > 0$ ,  $1 < \gamma_i < 2$  for  $i = 1, \dots, n$ . One feature that distinguishes this terminal manifold from those linear manifolds is that once  $s_i = 0$  is achieved, for any given initial condition  $e_i(t_0)$ ,  $i = 1, \dots, n$ ,  $e_i$  converges to zero in finite time  $t_{s,i} = \frac{\lambda_i^{(1/\gamma_i)}}{1-\frac{1}{\gamma_i}} |e_i(t_0)|^{(1-\frac{1}{\gamma_i})}$  [7]. It is noteworthy that Eq. (3) is essentially equivalent [7,13] to the fractional-order nonsingular terminal sliding manifold proposed in [4].

To utilize the attractive property of this sliding manifold, a feedback control law is needed to stabilize  $\mathbf{s} = \mathbf{0}$ . A widely adopted control structure is  $\mathbf{u} = \bar{\mathbf{u}}_{\text{eq}} + \mathbf{u}_s$ , where  $\bar{\mathbf{u}}_{\text{eq}}$  is a model-based estimation of the equivalent control [1,14], and  $\mathbf{u}_s$  is used to ensure the reachability of the sliding manifold. This model-based control structure is adopted by [14–21]. The physical meaning of the equivalent control is the control effort needed to maintain the sliding motion on the manifold, which requires  $\mathbf{s} = \dot{\mathbf{s}} = \mathbf{0}$  [1]. For the manifold given by Eq. (3), this requirement leads to:

$$\dot{\mathbf{s}} = \dot{\mathbf{e}} + \Lambda \Gamma \text{diag}(|\dot{\mathbf{e}}|^{\gamma-1}) \ddot{\mathbf{e}} = \mathbf{0} \quad (4)$$

where  $\Gamma = \text{diag}([\gamma_1, \dots, \gamma_n]^T)$ , and  $|\dot{\mathbf{e}}|^{\gamma-1} = [|\dot{e}_1|^{\gamma_1-1}, \dots, |\dot{e}_n|^{\gamma_n-1}]^T$ . For the output tracking problem, substituting Eq. (1) into Eq. (4) results in:

$$\begin{aligned} \dot{\mathbf{e}} + \Lambda \Gamma \text{diag}(|\dot{\mathbf{e}}|^{\gamma-1}) \\ \times \left( \frac{\partial \mathbf{G}_1 \mathbf{x}_2}{\partial \mathbf{x}_1} \mathbf{G}_1 \mathbf{x}_2 + \mathbf{G}_1 (\mathbf{f}_2 + \mathbf{G}_2 \mathbf{u}_{\text{eq}} + \mathbf{d}) - \ddot{\mathbf{y}}_r \right) = \mathbf{0} \end{aligned} \quad (5)$$

The exact value of  $\mathbf{u}_{\text{eq}}$  is unavailable since  $\mathbf{d}$  is unknown;  $\mathbf{f}_2$  and  $\mathbf{G}_2$  are also perturbed by uncertainties and faults. However, an estimation  $\bar{\mathbf{u}}_{\text{eq}}$  can be calculated based on the estimated models as:

$$\begin{aligned} \bar{\mathbf{u}}_{\text{eq}} &= (\mathbf{G}_1 \bar{\mathbf{G}}_2)^{-1} \\ &\times \left( \ddot{\mathbf{y}}_r - \Gamma^{-1} \Lambda^{-1} \text{sig}(\dot{\mathbf{e}})^{2-\gamma} - \frac{\partial \mathbf{G}_1 \mathbf{x}_2}{\partial \mathbf{x}_1} \mathbf{G}_1 \mathbf{x}_2 - \mathbf{G}_1 \bar{\mathbf{f}}_2 \right) \\ &\triangleq (\mathbf{G}_1 \bar{\mathbf{G}}_2)^{-1} \left( \mathbf{v}_{\text{eq}} - \frac{\partial \mathbf{G}_1 \mathbf{x}_2}{\partial \mathbf{x}_1} \mathbf{G}_1 \mathbf{x}_2 - \mathbf{G}_1 \bar{\mathbf{f}}_2 \right) \end{aligned} \quad (6)$$

$\mathbf{v}_{\text{eq}}$  in Eq. (6) denotes the equivalent virtual control, which is independent of the model information.  $\mathbf{u}_s$  is normally designed in form of  $\mathbf{u}_s = (\mathbf{G}_1 \bar{\mathbf{G}}_2)^{-1} \mathbf{v}_s$ , where the virtual control  $\mathbf{v}_s$  is inserted to achieve a desirable reaching law. In [4], the conventional design  $\mathbf{v}_s = -\mathbf{K}_s \text{sign}(\mathbf{s})$  is employed, which theoretically makes  $\mathbf{s}$  converge to zero in finite time if sufficiently high positive definite  $\mathbf{K}_s$  is used. However, the sign function is discontinuous, which causes chattering in practice [1,3]. Although the boundary-layer method is adopted in [4] to alleviate chattering, the finite-time convergence property is consequently lost. Moreover, only ultimate boundedness of  $\mathbf{s}$  can be achieved [4].

In view of the limitations of using the boundary-layer method, the fast-terminal-sliding-mode-type reaching law is proposed in [7], where  $\mathbf{v}_s = -\mathbf{K}_1 \mathbf{s} - \mathbf{K}_2 \text{sig}(\mathbf{s})^\rho$ ,  $\mathbf{K}_1 = \text{diag}([k_{1,1}, \dots, k_{1,n}]^T)$ ,  $k_{1,i} > 0$ ,  $\mathbf{K}_2 = \text{diag}([k_{2,1}, \dots, k_{2,n}]^T)$ ,  $k_{2,i} > \eta > 0$ , and  $\text{sig}(\mathbf{s})^\rho = [|s_1|^{p_1} \text{sign}(s_1), \dots, |s_n|^{p_n} \text{sign}(s_n)]^T$ ,  $0 < p_i = \rho < 1$ ,  $i = 1, \dots, n$ . This  $\mathbf{v}_s$  design is continuous without using any approximation. It also builds a bridge between the discontinuous reaching law (if  $\rho_i = 0$ , which causes chattering but leads to finite-time reaching) and the linear reaching law (if  $\rho_i = 1$ , which only achieves asymptotical convergence but is continuous). By requiring  $0 < \rho_i = \rho < 1$ ,  $i = 1, \dots, n$ , both finite-time reaching and continuity can be achieved [7]. In total, the NTSMC law for systems modeled by Eq. (1) is given by:

$$\begin{aligned} \mathbf{u}_{\text{nt}} &= \bar{\mathbf{u}}_{\text{eq}} + \mathbf{u}_s = (\mathbf{G}_1 \bar{\mathbf{G}}_2)^{-1} \left( \mathbf{v}_{\text{eq}} + \mathbf{v}_s - \frac{\partial \mathbf{G}_1 \mathbf{x}_2}{\partial \mathbf{x}_1} \mathbf{G}_1 \mathbf{x}_2 - \mathbf{G}_1 \bar{\mathbf{f}}_2 \right) \\ &= (\mathbf{G}_1 \bar{\mathbf{G}}_2)^{-1} \left( \ddot{\mathbf{y}}_r - \Gamma^{-1} \Lambda^{-1} \text{sig}(\dot{\mathbf{e}})^{2-\gamma} - \mathbf{K}_1 \mathbf{s} - \mathbf{K}_2 \text{sig}(\mathbf{s})^\rho \right. \\ &\quad \left. - \frac{\partial \mathbf{G}_1 \mathbf{x}_2}{\partial \mathbf{x}_1} \mathbf{G}_1 \mathbf{x}_2 - \mathbf{G}_1 \bar{\mathbf{f}}_2 \right) \end{aligned} \quad (7)$$

The dynamics of the sliding variable  $\mathbf{s}$  (Eq. (3)) under the control of Eq. (7) is given by:

$$\begin{aligned} \dot{\mathbf{s}} &= \dot{\mathbf{e}} + \Lambda \Gamma \text{diag}(|\dot{\mathbf{e}}|^{\gamma-1}) \ddot{\mathbf{e}} \\ &\times \left( \frac{\partial \mathbf{G}_1 \mathbf{x}_2}{\partial \mathbf{x}_1} \mathbf{G}_1 \mathbf{x}_2 + \mathbf{G}_1 \left( \mathbf{f}_2 + \mathbf{G}_2 (\mathbf{G}_1 \bar{\mathbf{G}}_2)^{-1} (\mathbf{v}_{\text{eq}} + \mathbf{v}_s \right. \right. \\ &\quad \left. \left. - \frac{\partial \mathbf{G}_1 \mathbf{x}_2}{\partial \mathbf{x}_1} \mathbf{G}_1 \mathbf{x}_2 - \mathbf{G}_1 \bar{\mathbf{f}}_2) + \mathbf{d} \right) - \ddot{\mathbf{y}}_r \right) \\ &\triangleq \dot{\mathbf{e}} + \Lambda \Gamma \text{diag}(|\dot{\mathbf{e}}|^{\gamma-1}) (\mathbf{v}_{\text{eq}} + \mathbf{v}_s + \mathbf{e}_{\text{nt}} - \ddot{\mathbf{y}}_r) \\ &= \Lambda \Gamma \text{diag}(|\dot{\mathbf{e}}|^{\gamma-1}) (\mathbf{e}_{\text{nt}} - \mathbf{K}_1 \mathbf{s} - \mathbf{K}_2 \text{sig}(\mathbf{s})^\rho) \end{aligned} \quad (8)$$

in which

$$\begin{aligned} \mathbf{e}_{\text{nt}} &= \mathbf{G}_1 (\mathbf{f}_2 - \bar{\mathbf{f}}_2) + ((\mathbf{G}_1 \mathbf{G}_2) (\mathbf{G}_1 \bar{\mathbf{G}}_2)^{-1} - \mathbf{I}) \\ &\times \left( \mathbf{v}_{\text{eq}} + \mathbf{v}_s - \frac{\partial \mathbf{G}_1 \mathbf{x}_2}{\partial \mathbf{x}_1} \mathbf{G}_1 \mathbf{x}_2 - \mathbf{G}_1 \bar{\mathbf{f}}_2 \right) + \mathbf{G}_1 \mathbf{d} \end{aligned} \quad (9)$$

represents the uncertainty vector remains in the closed-loop system.  $\mathbf{I} \in \mathbb{R}^{n \times n}$  is an identity matrix. This uncertainty/perturbation term is always assumed to be bounded in the literature (e.g., [14,22–25]) as a precondition of sliding mode control design.

Generally speaking, sliding mode control which depends on the model-based estimation of the equivalent control has a contradiction between the reduction of model dependency and the reduction of the resulting uncertainty. On the one hand, reducing the model dependency can simplify the implementation process and reduce the onboard computational load, but according to Eq. (9), a worse dynamic estimation leads to an increase in the remaining uncertainty. On the other hand, Eq. (9) shows that the reduction of uncertainty requires more accurate model estimations. Reducing the remaining uncertainty in the closed-loop system is important for SMC because the minimum possible SMC gains are positively correlated to the absolute values of the remaining uncertainties; reducing the SMC gains is beneficial to chattering reduction. This contradiction will be solved by a sensor-based design presented in the next subsection.

## 2.2. Incremental nonsingular terminal sliding model control

This subsection proposes the incremental nonsingular terminal sliding model control (INTSMC), which solves the contradiction in NTSMC by fully exploiting the sensor measurement. Denote the sampling interval as  $\Delta t$ . The first step of the INTSMC design is to derive the incremental dynamic equation by taking the first-order Taylor series expansion around the condition at  $t - \Delta t$  (denoted by the subscript 0) [11]. It can be seen from Eq. (1) that the relative degree [3,11] of the system equals two. Therefore, using Eqs. (1), (2), the incremental dynamics of  $\ddot{\mathbf{y}}$  are:

$$\begin{aligned} \ddot{\mathbf{y}} &= \frac{\partial \mathbf{G}_1 \mathbf{x}_2}{\partial \mathbf{x}_1} \mathbf{G}_1 \mathbf{x}_2 + \mathbf{G}_1 \mathbf{f}_2 + \mathbf{G}_1 \mathbf{G}_2 \mathbf{u} + \mathbf{G}_1 \mathbf{d} \\ &= \ddot{\mathbf{y}}_0 + \frac{\partial [\frac{\partial \mathbf{G}_1 \mathbf{x}_2}{\partial \mathbf{x}_1} \mathbf{G}_1 \mathbf{x}_2 + \mathbf{G}_1 \mathbf{f}_2 + \mathbf{G}_1 \mathbf{G}_2 \mathbf{u} + \mathbf{G}_1 \mathbf{d}]}{\partial \mathbf{x}} \Big|_0 \Delta \mathbf{x} \\ &\quad + (\mathbf{G}_1 \mathbf{G}_2) \Big|_0 \Delta \mathbf{u} + \frac{\partial [\mathbf{G}_1 \mathbf{f}_2 + \mathbf{G}_1 \mathbf{G}_2 \mathbf{u}]}{\partial \kappa} \Big|_0 \Delta \kappa + \mathbf{G}_{1,0} \Delta \mathbf{d} + \mathbf{R}_1 \end{aligned} \quad (10)$$

where  $\Delta \mathbf{x}$  and  $\Delta \mathbf{u}$  indicate the state and control increments in  $\Delta t$ .  $\Delta \kappa = \kappa - \kappa_0$  denotes the changes of the fault indicator  $\kappa$ , while  $\Delta \mathbf{d} = \mathbf{d} - \mathbf{d}_0$  denotes the variations of the external disturbances  $\mathbf{d}$  in  $\Delta t$ .  $\mathbf{R}_1$  in Eq. (10) is the expansion remainder, using Eqs. (1), (2), the Lagrange form of the remainder is:

$$\begin{aligned} \mathbf{R}_1 = & \frac{1}{2} \frac{\partial^2 [\frac{\partial \mathbf{G}_1 \mathbf{x}_2}{\partial \mathbf{x}_1} \mathbf{G}_1 \mathbf{x}_2 + \mathbf{G}_1 \mathbf{f}_2 + \mathbf{G}_1 \mathbf{G}_2 \mathbf{u} + \mathbf{G}_1 \mathbf{d}]}{\partial^2 \mathbf{x}} \Big|_m \Delta \mathbf{x}^2 \\ & + \frac{\partial \mathbf{G}_1 \mathbf{G}_2}{\partial \mathbf{x}} \Big|_m \Delta \mathbf{x} \Delta \mathbf{u} + \frac{\partial^2 [\mathbf{G}_1 \mathbf{f}_2 + \mathbf{G}_1 \mathbf{G}_2 \mathbf{u}]}{\partial \kappa \partial \mathbf{x}} \Big|_m \Delta \kappa \Delta \mathbf{x} \\ & + \frac{\partial \mathbf{G}_1}{\partial \mathbf{x}} \Big|_m \Delta \mathbf{d} \Delta \mathbf{x} + \frac{\partial \mathbf{G}_1 \mathbf{G}_1}{\partial \kappa} \Big|_m \Delta \mathbf{u} \Delta \kappa \end{aligned} \quad (11)$$

in which  $(\cdot)|_m$  means evaluating  $(\cdot)$  at a condition where  $\mathbf{x} \in (\mathbf{x}(t - \Delta t), \mathbf{x}(t))$ ,  $\mathbf{u} \in (\mathbf{u}(t - \Delta t), \mathbf{u}(t))$ ,  $\mathbf{d} \in (\mathbf{d}(t - \Delta t), \mathbf{d}(t))$ , and  $\kappa \in (\kappa(t - \Delta t), \kappa(t))$ . In Eq. (11),  $\mathbf{R}_1$  is not a function of  $\Delta \mathbf{u}^2$ ,  $\Delta \mathbf{d}^2$ ,  $\Delta \kappa^2$ , nor the coupling terms  $\Delta \kappa \Delta \mathbf{d}$ ,  $\Delta \mathbf{u} \Delta \mathbf{d}$ . This can be examined using Eqs. (1), (2).

Second, use the same sliding manifold as Eq. (3), and substitute Eq. (10) into Eq. (4) yields:

$$\begin{aligned} \dot{\mathbf{e}} + \Lambda \Gamma \text{diag}(|\dot{\mathbf{e}}|^{\gamma-1}) \\ \times \left( \ddot{\mathbf{y}}_0 + \frac{\partial [\frac{\partial \mathbf{G}_1 \mathbf{x}_2}{\partial \mathbf{x}_1} \mathbf{G}_1 \mathbf{x}_2 + \mathbf{G}_1 \mathbf{f}_2 + \mathbf{G}_1 \mathbf{G}_2 \mathbf{u} + \mathbf{G}_1 \mathbf{d}]}{\partial \mathbf{x}} \Big|_0 \Delta \mathbf{x} \right. \\ \left. + (\mathbf{G}_1 \mathbf{G}_2) \Big|_0 \Delta \mathbf{u} + \frac{\partial [\mathbf{G}_1 \mathbf{f}_2 + \mathbf{G}_1 \mathbf{G}_2 \mathbf{u}]}{\partial \kappa} \Big|_0 \Delta \kappa \right. \\ \left. + \mathbf{G}_{1,0} \Delta \mathbf{d} + \mathbf{R}_1 - \ddot{\mathbf{y}}_r \right) = \mathbf{0} \end{aligned} \quad (12)$$

Third, the equivalent control increments can be estimated from the algebraic Eq. (12) as:

$$\begin{aligned} \Delta \bar{\mathbf{u}}_{\text{eq}} = ((\mathbf{G}_1 \bar{\mathbf{G}}_2) \Big|_0)^{-1} \left( \ddot{\mathbf{y}}_r - \Gamma^{-1} \Lambda^{-1} \text{sig}(\dot{\mathbf{e}})^{2-\gamma} - \ddot{\mathbf{y}}_0 \right) \\ \triangleq ((\mathbf{G}_1 \bar{\mathbf{G}}_2) \Big|_0)^{-1} (\mathbf{v}_{\text{eq}} - \ddot{\mathbf{y}}_0) \end{aligned} \quad (13)$$

The equivalent virtual control  $\mathbf{v}_{\text{eq}}$  in Eq. (13) is the same as that in Eq. (6) for inserting the desired error dynamics.

**Remark 1.** In contrast to Eq. (6) which estimates the entire  $\bar{\mathbf{u}}_{\text{eq}}$ , Eq. (13) estimates the increments of  $\bar{\mathbf{u}}_{\text{eq}}$ . More importantly, Eq. (6) relies on the estimated model  $\bar{\mathbf{f}}_2$ , whereas Eq. (13) depends on  $\ddot{\mathbf{y}}_0$ , which can be directly measured [26,27] or estimated [28,29].

Then, for ensuring the reachability of  $\mathbf{s} = \mathbf{0}$ , the fast-terminal-sliding-mode-type reaching law is adopted, with  $\mathbf{v}_s = -\mathbf{K}_1 \mathbf{s} - \mathbf{K}_2 \text{sig}(\mathbf{s})^\rho$ .

Finally, the INTSMC law is proposed as

$$\begin{aligned} \Delta \mathbf{u}_{\text{int}} = \Delta \bar{\mathbf{u}}_{\text{eq}} + \Delta \mathbf{u}_s = ((\mathbf{G}_1 \bar{\mathbf{G}}_2) \Big|_0)^{-1} (\mathbf{v}_{\text{eq}} + \mathbf{v}_s - \ddot{\mathbf{y}}_0) \\ = ((\mathbf{G}_1 \bar{\mathbf{G}}_2) \Big|_0)^{-1} \left( \ddot{\mathbf{y}}_r - \Gamma^{-1} \Lambda^{-1} \text{sig}(\dot{\mathbf{e}})^{2-\gamma} - \mathbf{K}_1 \mathbf{s} \right. \\ \left. - \mathbf{K}_2 \text{sig}(\mathbf{s})^\rho - \ddot{\mathbf{y}}_0 \right) \end{aligned} \quad (14)$$

The entire control command for the actuator is  $\mathbf{u}_{\text{int}} = \Delta \mathbf{u}_{\text{int}} + \mathbf{u}_0$ , where  $\mathbf{u}_0$  is the actuator position measured at  $t - \Delta t$  [11]. Using Eq. (10), the dynamics of the sliding variable  $\mathbf{s}$  (Eq. (3)) under the control of Eq. (14) is given by:

$$\begin{aligned} \dot{\mathbf{s}} = \dot{\mathbf{e}} + \Lambda \Gamma \text{diag}(|\dot{\mathbf{e}}|^{\gamma-1})(\mathbf{v}_{\text{eq}} + \mathbf{v}_s + \mathbf{e}_{\text{int}} - \ddot{\mathbf{y}}_r) \\ = \Lambda \Gamma \text{diag}(|\dot{\mathbf{e}}|^{\gamma-1})(\mathbf{e}_{\text{int}} - \mathbf{K}_1 \mathbf{s} - \mathbf{K}_2 \text{sig}(\mathbf{s})^\rho) \end{aligned} \quad (15)$$

$\mathbf{e}_{\text{int}}$  in Eq. (15) is the lumped perturbation term, which is expressed as

$$\begin{aligned} \mathbf{e}_{\text{int}} = \delta(\mathbf{x}, \kappa, \Delta t) + ((\mathbf{G}_1 \mathbf{G}_2)(\mathbf{G}_1 \bar{\mathbf{G}}_2)^{-1} \Big|_0 - \mathbf{I})(\mathbf{v}_{\text{eq}} + \mathbf{v}_s - \ddot{\mathbf{y}}_0) \\ + \mathbf{G}_{1,0} \Delta \mathbf{d} \end{aligned} \quad (16)$$

1  $\|\mathbf{G}_{1,0}\| \|\Delta \mathbf{d}\| \leq \bar{G}_1 \overline{\Delta d}$  under Assumption 2. Because the variation  
2 terms are bounded under a sufficiently high  $f_s$ , analogous to the  
3 proof of Theorem 2 in [12],  $\varepsilon_{\text{int}}$  in Eq. (16) is bounded at each time  
4 step, and is ultimately bounded by  $\frac{\bar{G}_1 \Delta d + \Delta v b + \delta}{1 - b}$ .  $\square$   
5

6 **Lemma 1.** [7] Suppose  $a_1, a_2, \dots, a_n$  are positive numbers, and  $0 < p <$   
7 2, then  $(a_1^p + a_2^p + \dots + a_n^p)^p \leq (a_1^p + a_2^p + \dots + a_n^p)^2$ .  
8

9 **Lemma 2.** [7] If a Lyapunov function  $V$  satisfies  $\dot{V} + \alpha V + \beta V^\gamma \leq$   
10 0,  $\alpha, \beta > 0$ ,  $0 < \gamma < 1$ , then  $V = 0$  will be reached in finite time  
11  $T \leq \frac{1}{\alpha(1-\gamma)} \ln \frac{\alpha V^{1-\gamma}(t_0) + \beta}{\beta}$ .  
12

13 **Theorem 1.** For system modeled by Eq. (1) with sliding manifold given  
14 by Eq. (3), using the INTSMC designed as Eq. (14), then  
15

- 17 1. In the absence of the perturbation term  $\varepsilon_{\text{int}}$ ,  $\mathbf{s}$  and  $\mathbf{e}$  will converge  
18 to zero in finite time.
- 19 2. If the perturbation term  $\varepsilon_{\text{int}}$  (Eq. (16)) is bounded, then the sys-  
20 tem trajectories will converge to the neighborhood of  $\mathbf{s} = \mathbf{0}$  as  $s_i \leq$   
21  $\Delta_{\text{int},s_i} = (|\varepsilon_{\text{int},i}|/k_{2,i} - \eta)^{\frac{1}{\rho_i}}$  in finite time. Furthermore, the track-  
22 ing errors will converge to  $|e_i| \leq 2\Delta_{\text{int},s_i}$ , and  $|\dot{e}_i| \leq (\Delta_{\text{int},s_i}/\lambda_i)^{\frac{1}{\gamma_i}}$   
23 in finite time.
- 24

25 **Proof.** Consider the Lyapunov function  $V = \frac{1}{2} \mathbf{s}^T \mathbf{s}$ , the substitution  
26 of Eq. (15) yields  
27

$$\dot{V} = \mathbf{s}^T (\Lambda \Gamma \text{diag}(|\dot{\mathbf{e}}|^{\gamma-1}) (\varepsilon_{\text{int}} - \mathbf{K}_1 \mathbf{s} - \mathbf{K}_2 \text{sig}(\mathbf{s})^\rho)) \quad (21)$$

- 31 1. When  $\varepsilon_{\text{int}} = \mathbf{0}$ , Eq. (21) yields

$$\dot{V} = -\mathbf{s}^T \mathbf{K}_1 \mathbf{s} - \mathbf{s}^T \mathbf{K}_2 \text{sig}(\mathbf{s})^\rho \quad (22)$$

33 where  $\underline{\mathbf{K}}_1 = \Lambda \Gamma \text{diag}(|\dot{\mathbf{e}}|^{\gamma-1}) \mathbf{K}_1 = \text{diag}([\underline{k}_{1,1}, \dots, \underline{k}_{1,n}]^T)$  and  
34  $\underline{\mathbf{K}}_2 = \Lambda \Gamma \text{diag}(|\dot{\mathbf{e}}|^{\gamma-1}) \mathbf{K}_2 = \text{diag}([\underline{k}_{2,1}, \dots, \underline{k}_{2,n}]^T)$  are positive  
35 definite matrices if  $\dot{\mathbf{e}} \neq \mathbf{0}$ . Since  $0 < \rho_i = \rho < 1$ , using  
36 Lemma 1, then

$$\dot{V} \leq -2\underline{k}_1 V - 2^{(\rho+1)/2} \underline{k}_2 V^{(\rho+1)/2} \quad (23)$$

40 where  $\underline{k}_1 = \min\{\underline{k}_{1,i}\}$  and  $\underline{k}_2 = \min\{\underline{k}_{2,i}\}$ . According to Lem-  
41 ma 2,  $V$  will converge to zero in finite time  $T \leq \ln((\underline{k}_1 V(t_0)^{(1-\rho)/2} + 2^{(\rho-1)/2} \underline{k}_2)/(2^{(\rho-1)/2} \underline{k}_2))/(\underline{k}_1(1 - \rho))$ .  
42 Equivalently,  $\mathbf{s} = \mathbf{0}$  will be reached in finite time. Recall Eq. (3),  
43 on the terminal sliding surface,  $\mathbf{e}$  will converge to zero in fi-  
44 nite time.

45 The above analyses are based on  $\dot{\mathbf{e}} \neq \mathbf{0}$ . If at the reaching  
46 phase,  $s_i \neq 0$ , but  $\dot{e}_i = 0$ , then by using Eqs. (1), (7) the closed-  
47 loop system dynamics become:

$$\ddot{e}_i = -k_{1,i}s_i - k_{2,i}\text{sig}(s_i)^\rho \neq 0 \quad (24)$$

48 which means  $\dot{e}_i = 0$  is not an attractor in the reaching phase.  
49 Therefore, the finite-time reachability of the sliding manifold  
50 is still ensured.

- 52 2. When  $\varepsilon_{\text{int}} \neq \mathbf{0}$ , recall Eq. (22), Eq. (21) is written as:

$$\begin{aligned} \dot{V} &= -\mathbf{s}^T \underline{\mathbf{K}}_1 \mathbf{s} - \mathbf{s}^T \underline{\mathbf{K}}_2' \text{sig}(\mathbf{s})^\rho \\ &\quad + \mathbf{s}^T [\Lambda \Gamma \text{diag}(|\dot{\mathbf{e}}|^{\gamma-1}) (\varepsilon_{\text{int}} - (\mathbf{K}_2 - \eta \mathbf{I}) \text{sig}(\mathbf{s})^\rho)] \\ &= -\mathbf{s}^T \underline{\mathbf{K}}_1 \mathbf{s} - \mathbf{s}^T \underline{\mathbf{K}}_2' \text{sig}(\mathbf{s})^\rho \\ &\quad + \mathbf{s}^T [\Lambda \Gamma \text{diag}(|\dot{\mathbf{e}}|^{\gamma-1}) (\text{diag}(\varepsilon_{\text{int}}) \text{diag}^{-1}(\text{sig}(\mathbf{s})^\rho) \\ &\quad - (\mathbf{K}_2 - \eta \mathbf{I}) \text{sig}(\mathbf{s})^\rho)] \\ &\leq -\mathbf{s}^T \underline{\mathbf{K}}_1 \mathbf{s} - \mathbf{s}^T \underline{\mathbf{K}}_2' \text{sig}(\mathbf{s})^\rho, \end{aligned}$$

$$\forall |s_i| \geq \left( \frac{|\varepsilon_{\text{int},i}|}{k_{2,i} - \eta} \right)^{\frac{1}{\rho_i}} \triangleq \Delta_{\text{int},s_i} \quad (25)$$

67 where  $\underline{\mathbf{K}}_2' = \eta \Lambda \Gamma \text{diag}(|\dot{\mathbf{e}}|^{\gamma-1})$ . Using Lemma 1 and Lemma 2,  
68 Eq. (25) demonstrates that if  $\dot{\mathbf{e}} \neq \mathbf{0}$ ,  $s_i$  converges to the domain  
69 of  $s_i \leq \Delta_{\text{int},s_i}$  in finite time.

70 If  $\dot{\mathbf{e}} = \mathbf{0}$ , using Eqs. (1), (14) the closed-loop system dynamics  
71 become:

$$\ddot{e}_i = -k_{1,i}s_i - k_{2,i}\text{sig}(s_i)^\rho + \varepsilon_{\text{int},i} \quad (26)$$

72 which is nonzero outside the domain  $s_i \leq \Delta_{\text{int},s_i}$ . In other  
73 words,  $\dot{e}_i = 0$  is not an attractor in the reaching phase.

74 Furthermore, recall Eq. (3)

$$e_i + \lambda_i \text{sig}(\dot{e}_i)^{\gamma_i} = s_i \leq \Delta_{\text{int},s_i} \quad (27)$$

75 which can be rewritten as

$$e_i + \left( \lambda_i - \frac{s_i}{|\dot{e}_i|^{\gamma_i} \text{sign}(\dot{e}_i)} \right) |\dot{e}_i|^{\gamma_i} \text{sign}(\dot{e}_i) = 0 \quad (28)$$

76 Eq. (28) is still in the form of nonsingular terminal sliding  
77 mode if  $\lambda_i - s_i/|\dot{e}_i|^{\gamma_i} \text{sign}(\dot{e}_i) > 0$ , which means in finite time,  
78  $\dot{e}_i$  will converge to the domain:  
79

$$|\dot{e}_i| \leq \left( \frac{\Delta_{\text{int},s_i}}{\lambda_i} \right)^{\frac{1}{\gamma_i}} \quad (29)$$

80 Furthermore, using Eqs. (27), (29), it is derived that the fol-  
81 lowing inequalities are achieved in finite time:  
82

$$|e_i| \leq \lambda_i |\dot{e}_i|^{\gamma_i} + |s_i| \leq 2\Delta_{\text{int},s_i} \quad (30)$$

83 This completes the proof.  $\square$

84 Recall Eqs. (7), (8), the closed-loop system dynamics using  
85 NTSMC are:  $\dot{\mathbf{s}} = \Lambda \Gamma \text{diag}(|\dot{\mathbf{e}}|^{\gamma-1}) (\varepsilon_{\text{nt}} - \mathbf{K}_1 \mathbf{s} - \mathbf{K}_2 \text{sig}(\mathbf{s})^\rho)$ , which is  
86 in a similar form as Eq. (15) except the perturbation value. There-  
87 fore, the following Corollary of Theorem 1 can be derived for the  
88 model-based NTSMC:

89 **Corollary 1.** For system modeled by Eq. (1) with sliding manifold given  
90 by Eq. (3), using the NTSMC designed as Eq. (7), then

- 91 1. In the absence of the perturbation term  $\varepsilon_{\text{nt}}$ ,  $\mathbf{s}$  and  $\mathbf{e}$  will converge to  
92 zero in finite time.
- 93 2. If the perturbation term  $\varepsilon_{\text{nt}}$  (Eq. (9)) is bounded, then the system  
94 trajectories will converge to the neighborhood of  $\mathbf{s} = \mathbf{0}$  as  $s_i \leq$   
95  $\Delta_{\text{nt},s_i} = (|\varepsilon_{\text{nt},i}|/(k_{2,i} - \eta))^{\frac{1}{\rho_i}}$  in finite time. Furthermore, the track-  
96 ing errors will converge to  $|e_i| \leq 2\Delta_{\text{nt},s_i}$ , and  $|\dot{e}_i| \leq (\Delta_{\text{nt},s_i}/\lambda_i)^{\frac{1}{\gamma_i}}$  in  
97 finite time.

98 Although both NTSMC and INTSMC can make the system tra-  
99 jectories converge in finite time, they have different model depen-  
100 dency and robustness. These issues will be elaborated in the next  
101 subsection.

### 102 2.3. Comparisons between NTSMC and INTSMC

103 In this subsection, the model-based NTSMC method derived  
104 in 2.1 and the sensor-based INTSMC method proposed in 2.2 will  
105 be analytically compared.

106 First of all, by comparing Eq. (7) with Eq. (14), it can be seen  
107 that INTSMC replaces a part of the model information by sensor  
108 measurements. This reduction of model dependency can simplify

the implementation process, and reduce the onboard computational load.

Second of all, NTSMC and INTSMC result in different closed-loop perturbation terms, i.e.,  $\epsilon_{nt}$  and  $\epsilon_{int}$ . Generally speaking, the boundedness of the perturbation is the pre-condition of many robust control approaches, including sliding mode control. The sufficient conditions for the boundedness of  $\epsilon_{int}$  have been presented in Proposition 1. However, under the same conditions, the boundedness of  $\epsilon_{nt}$  is undetermined. In view of Eqs. (7), (9), the boundedness of  $\epsilon_{nt}$  requires  $\mathbf{G}_1(\mathbf{f}_f - \bar{\mathbf{f}}) + \mathbf{G}_1(\mathbf{G}_f - \bar{\mathbf{G}})\mathbf{u}_{nt}$  being bounded for all  $t$ , which is stricter than Assumption 4.

Third of all, even under the circumstances that both  $\epsilon_{nt}$  and  $\epsilon_{int}$  are bounded,  $\epsilon_{int}$  has lower upper bound than  $\epsilon_{nt}$ , which will be explained as follows:

Before a fault occurs, i.e.,  $t < t_f$ ,  $\kappa_0 = \kappa = 0$ ; using Eq. (9),  $\epsilon_{nt} = \mathbf{G}_1(\Phi\theta + \eta_f) + \mathbf{G}_1(\Psi\theta + \eta_G)\mathbf{u}_{nt} + \mathbf{G}_1\mathbf{d}$ ; using Eqs. (16), (19),  $\epsilon_{int} = \delta_b + (\mathbf{G}_1(\Psi\theta + \eta_G))|_0 \Delta\mathbf{u}_{int} + \mathbf{G}_{1,0}\Delta\mathbf{d}$ . For aerospace systems,  $\|\Phi\theta + \eta_f\|$  is normally large because of the difficulties in modeling the aerodynamic and inertia properties. On the contrary, since  $\|\Delta\mathbf{x}\|$  vanishes towards zero as  $\Delta t$  approaches zero, according to Eq. (19),  $\|\delta_b\|$  can become negligible under sufficiently high sampling frequency. Moreover, when  $\mathbf{u}_{nt} \neq \mathbf{0}$  and  $\mathbf{d} \neq \mathbf{0}$ , there exists an  $f_s$  such that  $\|\Delta\mathbf{u}_{int}\| \leq \|\mathbf{u}_{nt}\|$  and  $\|\Delta\mathbf{d}\| \leq \|\mathbf{d}\|$ . Therefore, when  $t < t_f$ , there exists an  $f_s$ , such that the upper bound of  $\epsilon_{int}$  is smaller than that of  $\epsilon_{nt}$ .

After a fault occurs, i.e.,  $t > t_f$ ,  $\kappa_0 = \kappa = 1$ , Eqs. (9), (16) show that  $\epsilon_{nt}$  is augmented by  $\mathbf{G}_1(\mathbf{f}_f - \bar{\mathbf{f}}_2) + \mathbf{G}_1(\mathbf{G}_f - \bar{\mathbf{G}}_2)\mathbf{u}_{nt}$ , which is fault-case dependent. By contrast, only  $\delta_d + \mathbf{G}_1(\mathbf{G}_f - \bar{\mathbf{G}}_2)\Delta\mathbf{u}_{int}$  is added to  $\epsilon_{int}$  as compared to the pre-fault condition. In spite of the fault cases, both  $\|\delta_d\|$  and  $\|\Delta\mathbf{u}_{int}\|$  approach zero as  $\Delta t$  decreases. In other words, as the sampling frequency increases, INTSMC becomes increasingly more robust to  $\epsilon_{int}$ .

In summary, under perturbed circumstances, there exists an  $f_s$  such that  $\epsilon_{int}$  has a lower upper bound than  $\epsilon_{nt}$ , both before and after a fault occurs. As a consequence, recall Theorem 1 and Corollary 1, if the same gains are used by NTSMC and INTSMC, the ultimate bounds of  $s_i$  and  $e_i$  are smaller using INTSMC. Moreover, to achieve the same tracking performance, because of the smaller bound of  $\epsilon_{int}$ , the required INTSMC gains are lower.  $\epsilon_{int}$  is also less fault-case dependent than  $\epsilon_{nt}$ . Based on the preceding discussions, it can be seen that INTSMC can simultaneously reduce the model dependency and the remaining uncertainty in NTSMC, thus the contradiction presented in subsection 2.1 is solved. The main reason that INTSMC can achieve enhanced robustness in spite of its reduced model dependency is its sensor-based control structure. As can be seen from Eqs. (16), (19), the main influences of uncertainties, disturbances, and faults are included in the measurements/estimations of  $\ddot{\mathbf{y}}_0$  and  $\mathbf{u}_0$ .

### 3. Quadrotor fault-tolerant control

In this section, the NTSMC and the INTSMC derived in Sec. 2 will be applied to quadrotor fault-tolerant control problems for robustness comparisons.

#### 3.1. Quadrotor dynamics

Fig. 1 shows a Parrot Bebop quadrotor.  $\mathcal{F}_I : (O_I, X_I, Y_I, Z_I)$  is the inertia frame, while  $\mathcal{F}_B : (O_B, X_B, Y_B, Z_B)$  indicates the body-fixed reference frame. Assume  $O_B$  is coincided with the center of mass.  $\omega = [\omega_1, \omega_2, \omega_3, \omega_4]^T$  indicates the rotor speeds with respect to  $\mathcal{F}_B$ . Denote the position and translational velocity vectors of  $\mathcal{F}_B$  with respect to  $\mathcal{F}_I$ , expressed in  $\mathcal{F}_I$ , as  $\mathbf{P} = [X, Y, Z]^T$  and  $\mathbf{V} = [V_x, V_y, V_z]^T$  respectively, then the translational dynamics of the quadrotor expressed in  $\mathcal{F}_I$  are:

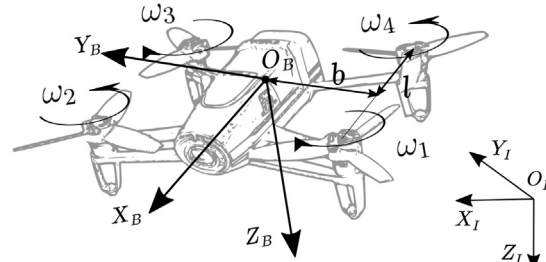


Fig. 1. The axes definition for a Parrot Bebop quadrotor.

$$\dot{\mathbf{P}} = \mathbf{V}$$

$$m\dot{\mathbf{V}} = m\mathbf{g} + \mathbf{L}_{IB}\mathbf{F}(\kappa) \quad (31)$$

where  $\mathbf{g} = [0, 0, g]^T$  is the gravitational acceleration vector,  $m$  is the mass, and  $\mathbf{L}_{IB}$  is the rotation matrix from  $\mathcal{F}_B$  to  $\mathcal{F}_I$ .  $\mathbf{F}(\kappa) = \mathbf{F}_a(\kappa) + \mathbf{F}_c(\kappa)$ , with  $\mathbf{F}_a$  indicates the aerodynamic force, and  $\mathbf{F}_c(\kappa) = [0, 0, -T(\kappa)]^T$  denotes the rotor thrust vector. The parameter  $\kappa$  (the same as that in Eq. (1b)) is used to model the influences of rotor faults. The rotational dynamics of the quadrotor expressed in  $\mathcal{F}_B$  are:

$$\dot{\boldsymbol{\eta}} = \mathbf{E}(\boldsymbol{\eta})\boldsymbol{\Omega} \quad (32a)$$

$$\mathbf{I}_v(\kappa)\dot{\boldsymbol{\Omega}} = -\tilde{\boldsymbol{\Omega}}\mathbf{I}_v(\kappa)\boldsymbol{\Omega} + \mathbf{M}(\kappa) \quad (32b)$$

where  $\boldsymbol{\eta} = [\phi, \theta, \psi]^T$  contains the Euler angles.  $\boldsymbol{\Omega} = [p, q, r]^T$  is the angular rate vector expressed in  $\mathcal{F}_B$ .  $(\cdot)$  indicates the skew symmetrical matrix of the vector  $(\cdot)$ .  $\mathbf{I}_v(\kappa)$  is the inertia matrix. The matrix  $\mathbf{E}(\boldsymbol{\eta})$  can be found in [30].  $\mathbf{M}(\kappa) = \mathbf{M}_a(\kappa) + \mathbf{M}_g(\kappa) + \mathbf{M}_c(\kappa)$ , with  $\mathbf{M}_a$ ,  $\mathbf{M}_g$ ,  $\mathbf{M}_c$  respectively represents the aerodynamic, gyroscopic, and control moment vector.

The thrust and reactive torque of the rotors are approximately proportional to  $\omega^2$  [28,31]. Denote the thrust coefficients of the four rotors as  $k_i$ ,  $i = 1, 2, 3, 4$ , and denote the reactive torque coefficients of the four rotors as  $\lambda_i$ ,  $i = 1, 2, 3, 4$ . Using the geometry parameters shown in Fig. 1,  $\mathbf{M}_c(\kappa)$  and the total thrust  $T(\kappa)$  are modeled by:

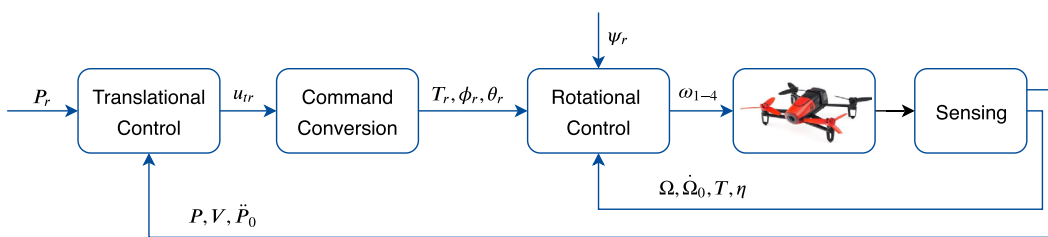
$$\begin{pmatrix} \mathbf{M}_c(\kappa) \\ \vdots \\ T(\kappa) \end{pmatrix} = \begin{pmatrix} -bk_1 & bk_2 & bk_3 & -bk_4 \\ lk_1 & lk_2 & -lk_3 & -lk_4 \\ \lambda_1 & -\lambda_2 & \lambda_3 & -\lambda_4 \\ \hline k_1 & k_2 & k_3 & k_4 \end{pmatrix} \omega^2 \triangleq \mathbf{G}_m(\kappa)\omega^2 \quad (33)$$

#### 3.2. Control structure

This paper considers quadrotor trajectory tracking control, namely the control aim is  $\mathbf{P} \rightarrow \mathbf{P}_r$ . The translational and rotational dynamics of the quadrotor obey the physical time-scale separation principle [8,21,32], which makes it feasible to design two cascaded control loops, as illustrated in Fig. 2.

##### Translational control:

The translational control considers Eq. (31), and aims at finding a reference for  $\mathbf{F}_c$  such that  $\mathbf{P} \rightarrow \mathbf{P}_r$  in finite time. In view of Eq. (31), define  $\mathbf{x}_1 = \mathbf{P}$ ,  $\mathbf{x}_2 = \mathbf{V}$ , and select  $\mathbf{u}_{tr} = \mathbf{L}_{IB}(\mathbf{F}_c/m)$ , then Eq. (31) is naturally in the form of Eq. (1) with  $n = 3$ ,  $\mathbf{G}_1 = \mathbf{G}_2 = I_{3 \times 3}$ ,  $\mathbf{f}_2 = \mathbf{g}$ ,  $\mathbf{d} = \mathbf{L}_{IB}(\mathbf{F}_a/m)$ . Moreover,  $\mathbf{G}_1$  is bounded and Assumption 1 is satisfied. Therefore, the NTSMC (Eq. (7)) and INTSMC (Eq. (14)) can be applied. According to Theorem 1 and Corollary 1, these two control methods ensure  $\mathbf{P} \rightarrow \mathbf{P}_r$  in finite time in the absence of perturbations, while making  $\mathbf{P}$  converges to the neighborhood of  $\mathbf{P}_r$  in the presence of bounded perturbations.

**Fig. 2.** Block diagram for control structure.**Table 1**

Inertia and geometric parameters of Parrot Bebop [31].

| $m$ [kg] | $I_x$ [kg·m <sup>2</sup> ] | $I_y$ [kg·m <sup>2</sup> ] | $I_z$ [kg·m <sup>2</sup> ] | $I_{xz}$ [kg·m <sup>2</sup> ] | $I_p$ [kg·m <sup>2</sup> ] | $b$ [m] | $l$ [m] | $R$ [m] |
|----------|----------------------------|----------------------------|----------------------------|-------------------------------|----------------------------|---------|---------|---------|
| 0.389    | 0.000906                   | 0.001242                   | 0.002054                   | 1.42E-05                      | 3.39E-06                   | 0.0775  | 0.0975  | 0.064   |

### Command conversion:

The control command for Euler angles  $\phi_r$ ,  $\theta_r$  and thrust  $T_r$  can be analytically solved from the algebraic equation  $\mathbf{u}_{tr} = \mathbf{L}_{IB}(\mathbf{F}_c/m)$ , where  $\mathbf{u}_{tr} = [u_1, u_2, u_3]^T$  is designed by the translational controllers. Using the expression of  $\mathbf{L}_{IB}$  [30], then

$$\begin{aligned} T_r &= \|\mathbf{u}_{tran}\|_2 = \sqrt{u_1^2 + u_2^2 + u_3^2} \\ \phi_r &= \arcsin\left(-\left(\frac{m}{T_r}\right)(u_1 \sin \psi - u_2 \cos \psi)\right) \\ \theta_r &= \arcsin\left(\frac{-(mu_1)/T_r - \sin \psi \sin \phi_r}{\cos \phi_r \cos \psi}\right) \end{aligned} \quad (34)$$

The heading angle command  $\psi_r$  can be assigned independent of the trajectory commands.

### Rotational control:

The inner-loop control aims at  $\eta \rightarrow \eta_r = [\phi_r, \theta_r, \psi_r]^T$  and  $T/m \rightarrow T_r/m$ . Eqs. (32b), (33) are incorporated as:

$$\begin{pmatrix} \dot{\Omega} \\ T/m \end{pmatrix} = \begin{pmatrix} -\mathbf{I}_v^{-1} \tilde{\Omega} \mathbf{I}_v \Omega \\ 0 \end{pmatrix} + \begin{pmatrix} \mathbf{I}_v^{-1} & \mathbf{0}_{3 \times 1} \\ \mathbf{0}_{1 \times 3} & 1/m \end{pmatrix} \mathbf{G}_m \omega^2 + \begin{pmatrix} \mathbf{I}_v^{-1} \mathbf{M}_a + \mathbf{I}_v^{-1} \mathbf{M}_g \\ 0 \end{pmatrix} \quad (35)$$

where  $\mathbf{0}_{p \times q}$  is a  $p \times q$  dimensional zero matrix. The inner-loop control command is chosen as  $\mathbf{u} = \omega^2$  in this paper, which allows the uncertainties and faults in  $\mathbf{G}_m$  (Eq. (33)) being considered in the controller design. By contrast, the common choice [5,15,17,33, 34] of  $\mathbf{u} = [\mathbf{M}_c, T]^T$  can only compensate for the uncertainties in  $\mathbf{I}_v$  and  $m$ . Eq. (35) is in the form of Eq. (1b) with  $\mathbf{x}_2 = [\Omega, \int T/m]^T$ . The disturbance vector  $\mathbf{d}$  equals  $[\mathbf{I}_v^{-1}(\mathbf{M}_a + \mathbf{M}_g), 0]^T$ . Eq. (32a) belongs to Eq. (1a) when choosing  $\mathbf{x}_1 = [\eta, \int \int T/m]^T$ , and  $\mathbf{G}_1 = \text{diag}\{\mathbf{E}(\eta), 1\}$ . It can be seen from the expression of  $\mathbf{E}(\eta)$  [30] that  $\mathbf{G}_1$  is nonsingular and bounded when the pitch angle  $\theta \in (-\frac{\pi}{2}, \frac{\pi}{2})$ . Therefore, applying NTSMC (Eq. (7)) or INTSMC (Eq. (14)) control enforces  $(\eta - \eta_r) \rightarrow 0$ ,  $\int \int (T - T_r)/m \rightarrow 0$  in finite time in the absence of perturbations, while making  $\eta$ ,  $\int \int T/m$  converge to the neighborhood of their references in the presence of perturbations. It is noteworthy that  $\int \int (T - T_r)/m \rightarrow 0$  is a sufficient condition for  $T/m \rightarrow T_r/m$ .

In this quadrotor flight control scheme, the number of inner-loop states ( $\Omega, \int T/m$ ) equals four, which is identical to the number of control inputs. If the number of control inputs is larger than four (e.g., hexacopters and octocopters), the current scheme can be used along with a control allocation method. If the number of control inputs becomes smaller than four (e.g., three-rotor aircraft), the present control scheme can be used along with the reduced-attitude control strategy [29].

**Table 2**

Dynamics and control parameters used by NTSMC (Eq. (7)) and INTSMC (Eq. (14)).

| Parameters     | Translational loop                                   | Rotational loop  |
|----------------|--|--|
| $\mathbf{G}_1$ | $\mathbf{I}_{3 \times 3}$                            | $\text{diag}\{\mathbf{E}(\eta), 1\}$                         |
| $\mathbf{G}_2$ | $\mathbf{I}_{3 \times 3}$                            | $\text{diag}(\mathbf{I}_v^{-1}, 1/m)$                        |
| $\mathbf{f}_2$ | $\mathbf{g}$   | $[-\mathbf{I}_v^{-1} \tilde{\Omega} \mathbf{I}_v \Omega; 0]$ |
| $\Lambda$      | $\Lambda_{tr} = \text{diag}([2, 2, 1]^T)$            | $\Lambda_{ro} = \text{diag}([1, 1, 1, 1]^T)$                 |
| $\gamma$       | $\gamma_{tr} = [7/5, 7/5, 7/5]^T$                    | $\gamma_{ro} = [5/3, 5/3, 5/3, 5/3]^T$                       |
| $\mathbf{K}_1$ | $\mathbf{K}_{1,tr} = \text{diag}([1, 1, 1]^T)$       | $\mathbf{K}_{1,ro} = \text{diag}([15, 15, 7.5, 15]^T)$       |
| $\mathbf{K}_2$ | $\mathbf{K}_{2,tr} = \text{diag}([0.6, 0.6, 0.6]^T)$ | $\mathbf{K}_{2,ro} = \text{diag}([5, 5, 2.5, 5]^T)$          |
| $\rho$         | $\rho_{tr} = 0.6$                                    | $\rho_{ro} = 0.5$  |

### 4. Numerical validation

In this section, the controllers designed in Sec. 2 and Sec. 3 will be tested in the Matlab/Simulink environment. Two Parrot Bebop models are used in this paper, namely one high fidelity model for simulations and another simplified model used for control design. The nominal geometric and inertia parameters of Parrot Bebop are summarized in Table 1. The high fidelity model contains the aerodynamic and gyroscopic effects identified from wind tunnel test data [31]. This model also includes actuator dynamics and nonlinear limits. The actuator dynamics are modeled as first-order low-pass filters with time constants of 0.02 s. The maximum and minimum rotational speed of the rotors are 1200 rad/s and 300 rad/s respectively. Moreover, the inertia, aerodynamic, and control effectiveness parameters are all functions of  $\kappa(t)$  in the high fidelity model, such that the influences of sudden actuator faults are included. The NTSMC (Eq. (7)) uses the estimated models  $\bar{\mathbf{f}}_2$  and  $\bar{\mathbf{G}}_2$ , whereas the INTSMC (Eq. (14)) only requires  $\bar{\mathbf{G}}_2$ . By contrast, the simplified model ( $\bar{\mathbf{f}}_2$ ,  $\bar{\mathbf{G}}_2$ ) used by the controllers excludes the aerodynamic, gyroscopic, and actuator effects, and is also kept invariant in the presence of rotor faults. In this way the robustness of the controllers to model uncertainties, disturbances and faults can be tested. The simulation sampling frequency is 500 Hz.

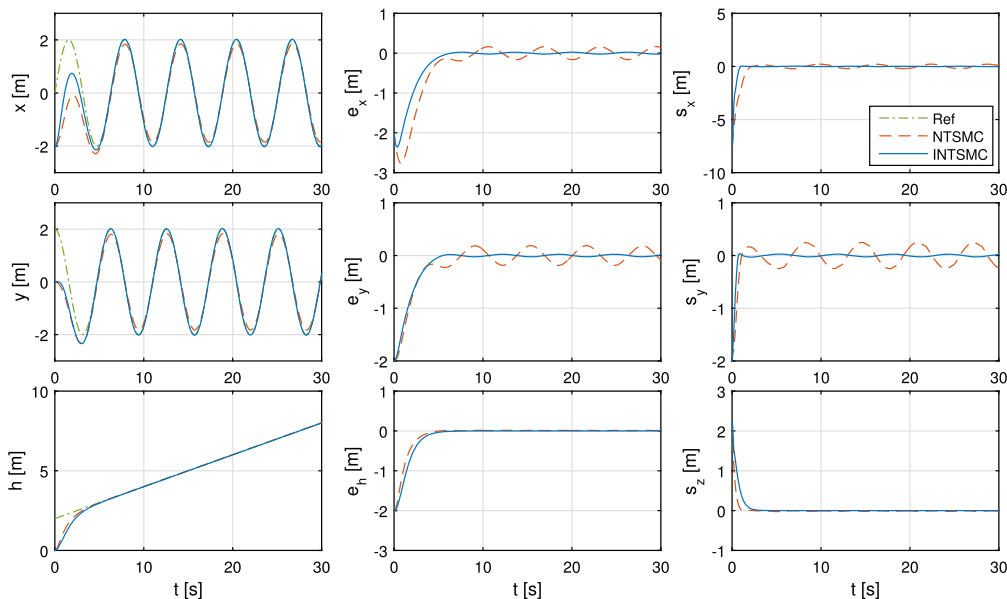
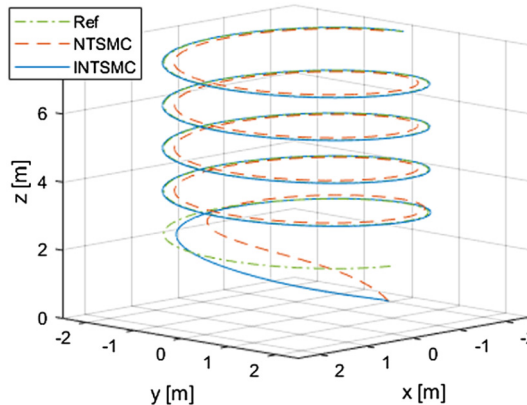
Based on the discussions in Sec. 3, both the translational and rotational dynamics of a quadrotor are in the form of Eq. (1), thus the NTSMC given by Eq. (7) and the INTSMC designed as Eq. (14) can be applied. For fair comparisons, the control parameters used by NTSMC and INTSMC are first kept identical. Gain adjustments and their consequences will be discussed in subsection 4.4. The dynamic matrices and the control parameters used by the controllers are summarized in Table 2.

In the following subsections, the robustness of NTSMC and INTSMC to model uncertainties, gusts and sudden actuator faults will be evaluated. The simulation scenarios are summarized in Table 3. In subsection 4.1, the quadrotor trajectory tracking in the presence of parametric uncertainties and unmodeled dynamics will be considered. The robustness of INTSMC and NTSMC will be compared. The tracking difficulty increases in subsection 4.2, where gust disturbances present. In subsection 4.3, the trajectory track-

**Table 3**

Simulations cases in subsections 4.1–4.4.

| Sec. | Simulation Scenarios  | Compare INTSMC with |
|------|---|---------------------|
| 4.1  | Scenario 1: uncertainties and unmodeled dynamics                          | NTSMC               |
| 4.2  | Scenario 2: uncertainties, unmodeled dynamics, and gusts                  | NTSMC               |
| 4.3  | Scenario 3: uncertainties, unmodeled dynamics, gusts, and actuator faults | NTSMC               |
| 4.4  | Scenario 3: uncertainties, unmodeled dynamics, gusts, and actuator faults | High-gain NTSMC     |

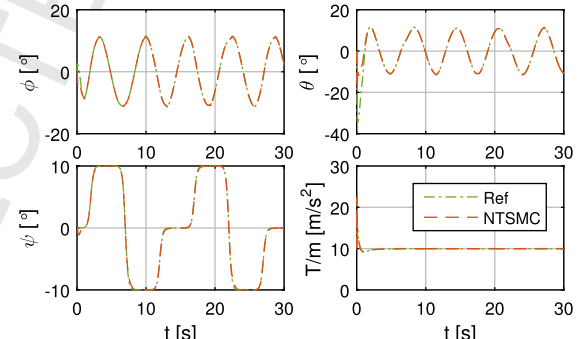
**Fig. 4.** Position responses in the presence of model uncertainties (Scenario 1).**Fig. 3.** 3D trajectory responses in the presence of model uncertainties (Scenario 1).

ing becomes even more challenging, where sudden actuator faults occur during flight. It will be shown in subsection 4.3 that NTSMC leads to instability in Scenario 3, while INTSMC can execute the task in spite of actuator faults. To rescue the quadrotor using NTSMC, the control gains are raised in subsection 4.4. However, it will be revealed in subsection 4.4 that even though high-gain NTSMC can stabilize the system, corresponding side-effects also emerge.

#### 4.1. Robustness to parametric uncertainties and unmodeled dynamics

**Scenario 1:** Trajectory tracking in the presence of parametric uncertainties and unmodeled dynamics.

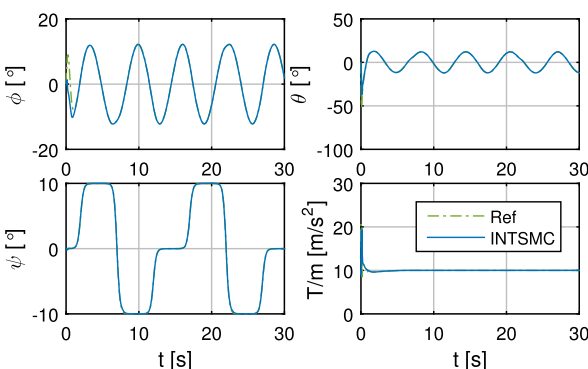
The unmodeled dynamics include the aerodynamics, gyroscopic effects and actuator dynamics, which are unknown by the controllers. To model the parametric uncertainties, the parameters used by the controllers are equal to the nominal (in the hover con-

**Fig. 5.** Attitude and thrust tracking performance using NTSMC in Scenario 1.

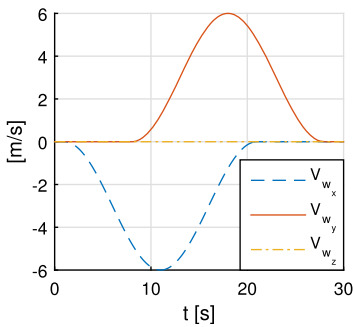
dition without fault) parameters multiplied with uncertain coefficients. To be specific, in the following simulations, the estimated parameters are:  $\bar{\mathbf{I}}_v = \text{diag}([1.5, 1.3, 0.7]^T) \cdot \mathbf{I}_v$ ,  $\bar{b} = 0.8b$ ,  $\bar{l} = 0.6l$ ,  $\bar{m} = 1.5m$ ,  $\bar{\lambda}_i = 0.6\lambda_i$ ,  $\bar{k}_i = 1.5k_i$ ,  $i = 1, 2, 3, 4$ .

Fig. 3 shows the three dimensional tracking trajectories under the control of NTSMC and INTSMC, with an initial position error  $\mathbf{e}_p(t=0) = [-2, -2, -2]^T$  m, and an initial velocity  $\mathbf{V}(t=0) = \mathbf{0}$  m/s. As can be seen from Fig. 3, although both NTSMC and INTSMC can make the quadrotor follow the spiral trajectory command in Scenario 1, INTSMC shows better tracking performance. This conclusion is further supported by Fig. 4, where INTSMC accomplishes  $\|\mathbf{e}_P\| = [\mathbf{e}_x, \mathbf{e}_y, \mathbf{e}_z]^T \leq 0.058$  m within 5.9 s, and the sliding variables  $\|\mathbf{s}_p\| = [s_x, s_y, s_z]^T \leq 0.066$  m within 2.2 s, whereas NTSMC can only achieve  $\|\mathbf{e}_P\| \leq 0.50$  m and  $\|\mathbf{s}_p\| \leq 0.58$  m. The errors in the position tracking are mainly caused by the aerodynamic forces  $\mathbf{F}_a$  and model uncertainties.

The outer-loop control of NTSMC and INTSMC give different references for the inner-loop controllers, as respectively displayed in Fig. 5 and Fig. 6. Although the inner-loop tracking performance, af-



**Fig. 6.** Attitude and thrust tracking performance using INTSMC in Scenario 1.



**Fig. 7.** Gust velocities in the inertial frame.

ter  $t = 1.5$  s are comparable in Figs. 5 and 6, the quadrotor using INTSMC responds faster in the transient phase. The heading angle command  $\psi_r$  is designed as smoothly combined sigmoid functions, which is independent of the position commands.

#### 4.2. Robustness to uncertainties and external disturbances

Scenario 2: Trajectory tracking in the presence of parametric uncertainties, unmodeled dynamics, and gusts.

In contrast to Scenario 1, gusts are included in Scenario 2. The airspeed of the quadrotor  $\mathbf{V}_a$  is a summation of ground speed  $\mathbf{V}$  and gust speed  $\mathbf{V}_w$ . "1-cos" gusts [35] are added along the x and y directions of the inertial frame, with  $\|\mathbf{V}_w\|_\infty = 6$  m/s as shown in Fig. 7. The simulations use a high fidelity aerodynamic model identified from wind tunnel test data [31], and the resulting aerodynamic forces and moments are viewed as disturbances by the onboard controllers.

Fig. 8 reveals that the tracking performance of NTSMC is noticeably reduced by the wind disturbance, whereas the performance of INTSMC is hardly influenced. This is also verified in Fig. 9, which shows that the quadrotor equipped with NTSMC leads to  $\max |s_x| = 1.30$  m,  $\max |s_y| = 1.41$  m,  $\max |s_z| = 0.42$  m, whereas the quadrotor using INTSMC remains in the region  $\|\mathbf{s}_p\| \leq 0.091$  m. The tracking error  $\mathbf{e}_p$  using NTSMC presents  $\max |e_x| = 1.15$  m at  $t = 14.1$  s, and  $\max |e_y| = 1.31$  m around  $t = 21.5$  s, as disturbed by the horizontal gust. On the contrary, INTSMC has better disturbance rejection ability since  $\|\mathbf{e}_p\| \leq 0.059$  m after  $t = 5.9$  s.

The inner-loop tracking responses are plotted in Figs. 10 and 11. When compared to Figs. 5 and 6, the  $\phi_r$ ,  $\theta_r$  in Figs. 10 and 11 present additional low frequency component in Scenario 2. These low frequency commands help the quadrotor to compensate for the influences of gusts. Although the gusts impose both disturbing  $\mathbf{F}_a$  and  $\mathbf{M}_a$  on the quadrotor,  $\mathbf{M}_a$  is less influential than  $\mathbf{F}_a$  [31]. Consequently, NTSMC and INTSMC show comparable inner-loop tracking performance in Scenario 2, as shown in Figs. 10 and 11.

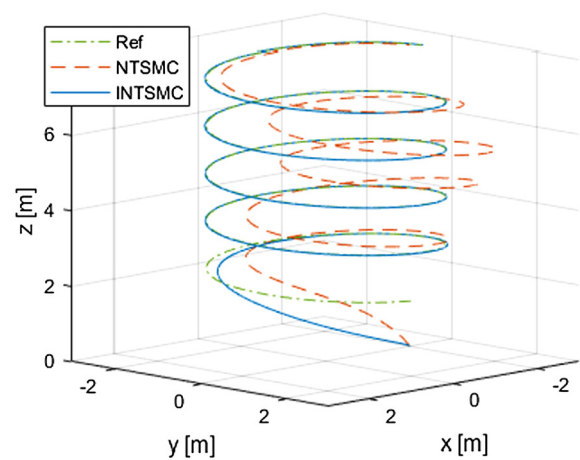


**Fig. 8.** 3D trajectory responses in the presence of model uncertainties and gusts (Scenario 2).

The core of the better robustness of INTSMC has been revealed in subsection 2.3; the sensor-based feature of INTSMC makes the upper bound of  $\epsilon_{int}$  smaller than that of  $\epsilon_{nt}$ , in the presence of bounded disturbances. This argument is verified by Fig. 12, which presents the outer-loop residual errors  $\epsilon_{V_x}$ ,  $\epsilon_{V_y}$ ,  $\epsilon_{V_z}$ . By virtue of the sensor-based control structure of INTSMC, the main influences of external disturbances are contained in the measurements/estimations of  $\ddot{\mathbf{y}}_0$  and  $\mathbf{u}_0$ , thus only  $\Delta\mathbf{d}$  presents in Eq. (16).

#### 4.3. Robustness to uncertainties, external disturbances, and sudden actuator faults

When compared to Scenario 2, successive actuator faults are added to Scenario 3. To model a sudden fault of the  $i$ -th rotor during flight, for  $t \geq t_f$ , the corresponding effectiveness in  $\mathbf{G}_m$  (Eq. (33)) is scaled in the simulation model, i.e.,  $k'_i = \mu_i k_i$ ,  $\lambda'_i = \mu_i \lambda_i$ ,  $\mu_i \in (0, 1]$  [36]. The aerodynamic and gyroscopic forces/moment are also influenced by rotor faults. For testing the robustness, constant  $\bar{\mathbf{G}}_m$  and  $\bar{\mathbf{I}}_v$  are consistently used by both controllers in spite of faults.

Scenario 3: Trajectory tracking in the presence of parametric uncertainties, unmodeled dynamics, gusts, and actuator faults.  $\mu_{1-4} = 1$  when  $0 \leq t < 10$  s,  $\mu_1 = 0.5$ ,  $\mu_{2-4} = 1$  when  $10 \leq t < 15$  s,  $\mu_{1-2} = 0.5$ ,  $\mu_{3-4} = 1$  when  $15 \leq t < 20$  s,  $\mu_{1-3} = 0.5$ ,  $\mu_4 = 1$  when  $20 \leq t < 25$  s, and finally  $\mu_{1-4} = 0.5$  when  $25 \leq t \leq 30$  s.

Fig. 13 illustrates the tracking performance of NTSMC and INTSMC in Scenario 3. Fig. 13 shows that the quadrotor which uses NTSMC crashes, whereas INTSMC drives the quadrotor along the reference trajectory in spite of uncertainties, disturbances, and successive actuator faults. The responses of the outer-loop tracking and sliding variables are presented in Fig. 14, in which the quadrotor using NTSMC significantly losses height after the first rotor fault occurs at  $t = 10$  s. For clarity, only the responses before  $t = 15$  s are plotted for NTSMC. On the contrary, INTSMC makes  $\|\mathbf{e}_p\| \leq 0.059$  m within 5.9 s, and  $\|\mathbf{s}_p\| \leq 0.068$  m within 2.2 s in Scenario 3.

The inner-loop responses are presented in Fig. 15, which indicates that the model-based NTSMC becomes unstable after the first rotor breaks at  $t = 10$  s. By contrast, the sensor-based INTSMC is able to maintain stability and desirable tracking performance. It can be seen from Fig. 16 that only small ripples are present around  $t = 10, 15, 20, 25$  s, and  $\|\mathbf{e}_T\| \leq 0.071^\circ$ ,  $|e_{T/m}| \leq 0.001$  m/s<sup>2</sup> can be recovered within 1.5 s after faults occur.

The instability of NTSMC is further illustrated in Figs. 17 and 18, where the rotor speed, and inner-loop residual errors have severe oscillations, and eventually diverge. As opposed to this, when using INTSMC, the damaged rotors speed up rapidly after faults occur

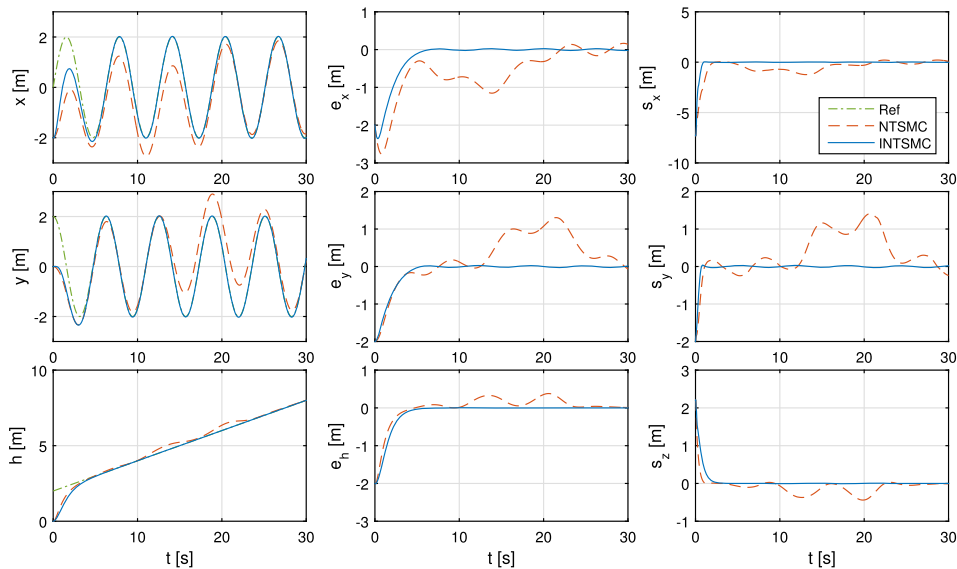


**Fig. 9.** Position responses in the presence of model uncertainties and gusts (Scenario 2).

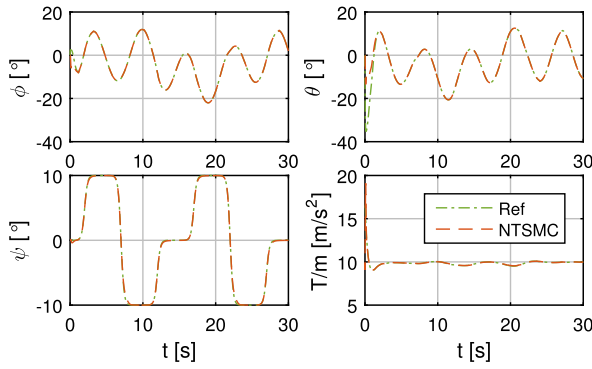


**Fig. 10.** Attitude and thrust tracking performance using NTSMC in Scenario 2.

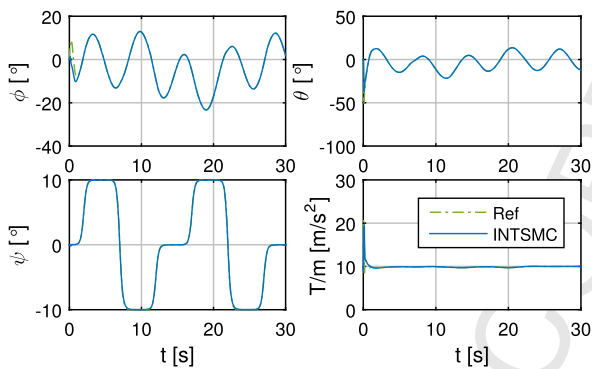


**Fig. 11.** Attitude and thrust tracking performance using INTSMC in Scenario 2.

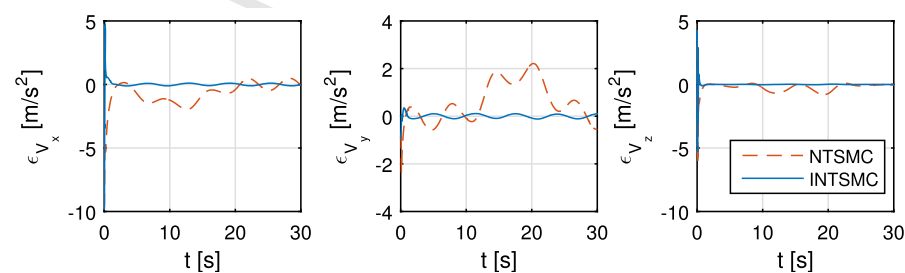


**Fig. 12.** Responses of  $\epsilon_{v_x}$ ,  $\epsilon_{v_y}$ ,  $\epsilon_{v_z}$  using NTSMC and INTSMC in Scenario 2.

(Fig. 17), which automatically compensates for the control effectiveness losses. The inner-loop residual errors using INTSMC also remain bounded after faults occur, as illustrated in Fig. 18.

#### 4.4. High-gain NTSMC

According to Corollary 1, in the presence of perturbations, NTSMC is stable if  $\epsilon_{nt}$  is bounded. However, from Eq. (9),  $\epsilon_{nt}$  is a function of the control input  $u$ ; therefore, its boundedness cannot be determined before the closure of the control loop. For

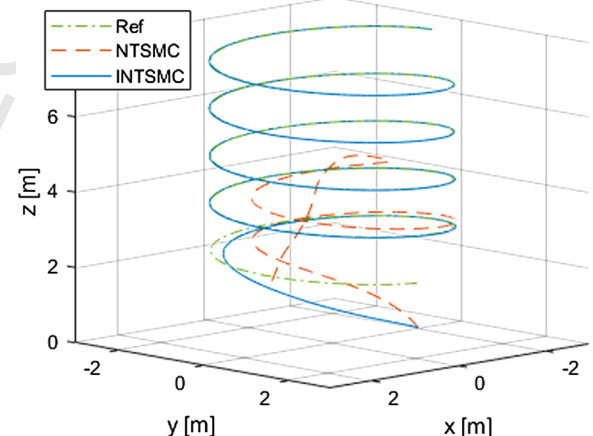


**Fig. 13.** 3D trajectory responses in the presence of uncertainties, disturbances, and successive actuator faults at  $t = 10, 15, 20, 25$  s (Scenario 3).

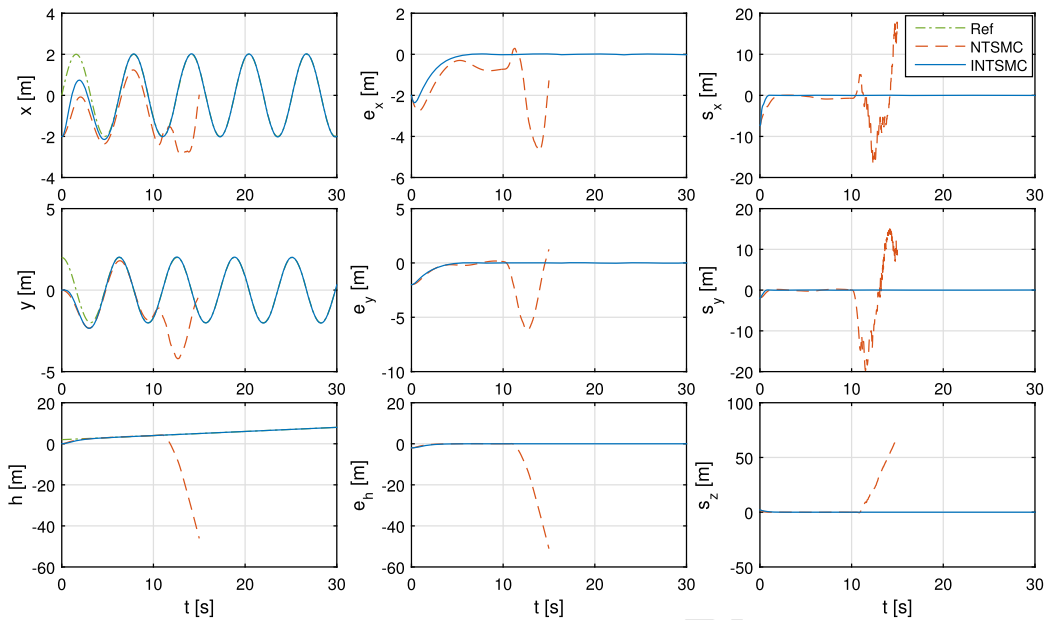


**Fig. 14.** Position responses in the presence of uncertainties, disturbances, and successive actuator faults at  $t = 10, 15, 20, 25$  s (Scenario 3).

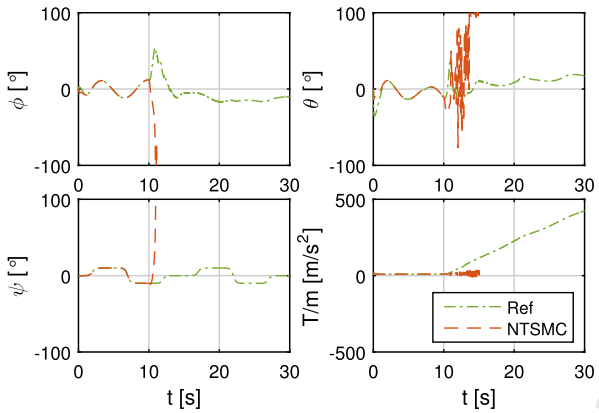


**Fig. 15.** Attitude and thrust tracking performance using NTSMC in Scenario 3.

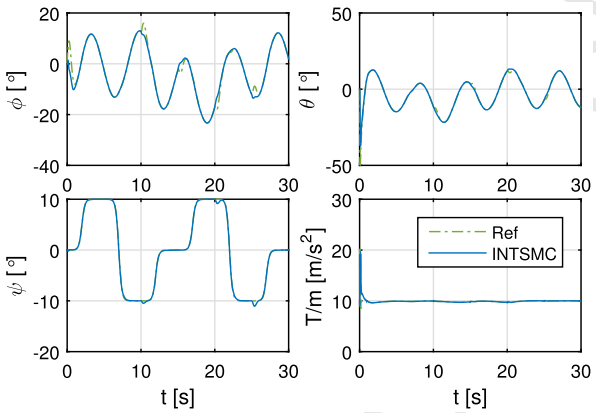


**Fig. 16.** Attitude and thrust tracking performance using INTSMC in Scenario 3.

the feasibility of controller design,  $\epsilon_{nt}$  is assumed to be bounded in [14,22–25]. However, as can be seen from Fig. 18,  $\epsilon_{nt}$  using the present control parameters becomes unbounded in Scenario 3.

In view of the preceding subsection, the instability of NTSMC is mainly caused by the inner-loop instability induced by rotor faults. An instinctive approach to rescue NTSMC is raising the inner-

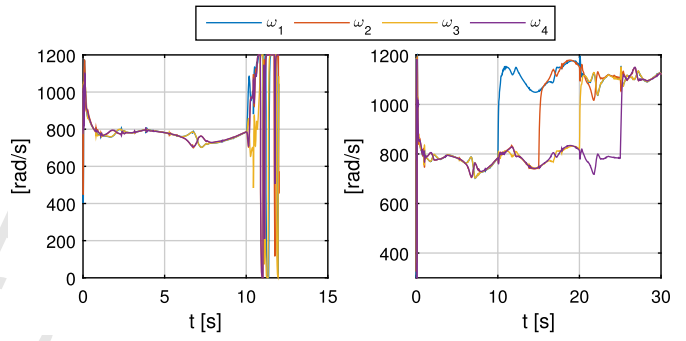


**Fig. 17.** Rotor speeds using NTSMC (left) and INTSMC (right) in Scenario 3.

loop control gains. Selecting  $K_{1,ro} = c_1 \cdot \text{diag}([15, 15, 7.5, 15]^T)$ , and  $K_{2,ro} = c_2 \cdot \text{diag}([5, 5, 2.5, 5]^T)$ , where  $c_1, c_2 > 1$ . For Scenario 3, based on the simulation results, the lowest gain coefficients that can result in a stable system are  $c_1 = 12$ ,  $c_2 = 20$ , with the inner-loop uncertainties shown in Fig. 19.

NTSMC with  $c_1 = 12$ ,  $c_2 = 20$  will be referred to as very-high-gain (VHG) NTSMC. Fig. 19 shows  $\epsilon_{nt}$  in the rotational loop becomes bounded using the VHG-NTSMC. Moreover,  $\epsilon_{nt}$  shows steep variations at  $t = 10, 15, 20, 25$  s. Referring to the analyses in subsection 2.3, these steep variations are caused by the term  $G_1(f_f - \bar{f}_2) + G_1(G_f - \bar{G}_2)\mathbf{u}_{nt}$ . More importantly, Fig. 19 illustrates that  $\|\epsilon_{nt}\|$  is significantly smaller than  $\|\epsilon_{nt}\|$  in Scenario 3, this verifies the analyses in subsection 2.3.

However, NTSMC with very high control gains has side-effects. As illustrated in Fig. 20, the rotor speeds using VHG-NTSMC show severe oscillations. These oscillations/chattering are present near the sliding surfaces, as can be seen from the inner-loop sliding variable responses in Fig. 21. It is worth noting that even though the control input given by Eq. (7) is continuous, chattering does occur when the very-high-gain controller is applied with limited-bandwidth actuators. In practice, very high control gains also amplify measurement noise. The chattering phenomenon can be mitigated by introducing gain adaption mechanisms [37,38], such that the control gains can be automatically reduced near the sliding surfaces, and be increased when perturbations are large. Nevertheless, when  $\epsilon_{nt}$  has steep variations caused by sudden faults

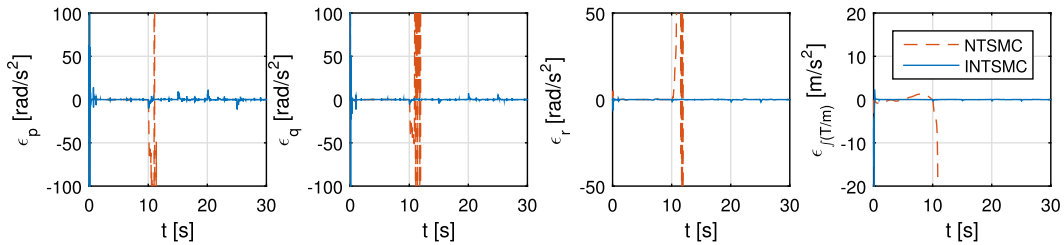
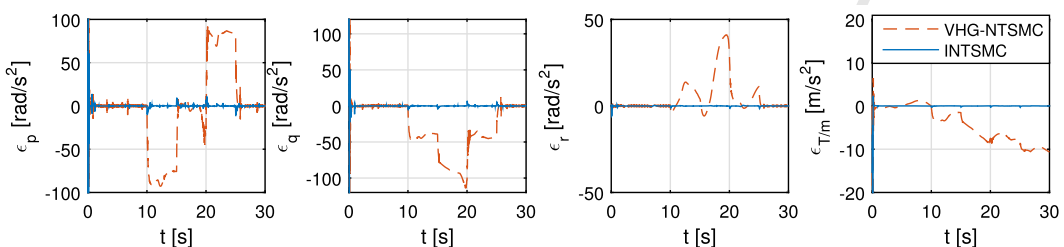
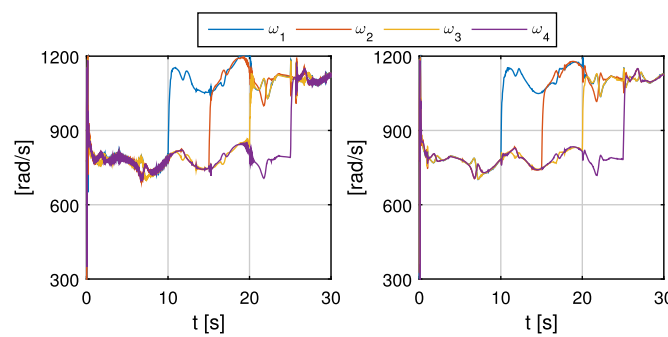
Fig. 18. Responses of  $\epsilon_p$ ,  $\epsilon_q$ ,  $\epsilon_r$ ,  $\epsilon_{f T/m}$  using NTSMC and INTSMC in Scenario 3.Fig. 19. Responses of  $\epsilon_p$ ,  $\epsilon_q$ ,  $\epsilon_r$ ,  $\epsilon_{f T/m}$  using VHG-NTSMC and INTSMC in Scenario 3.

Fig. 20. Rotor speeds using VHG-NTSMC (left) and INTSMC (right) in Scenario 3.

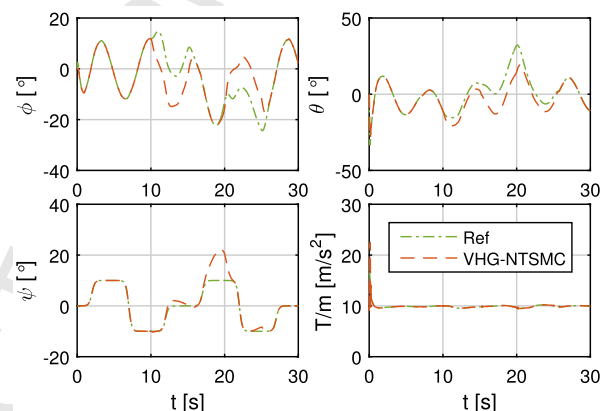
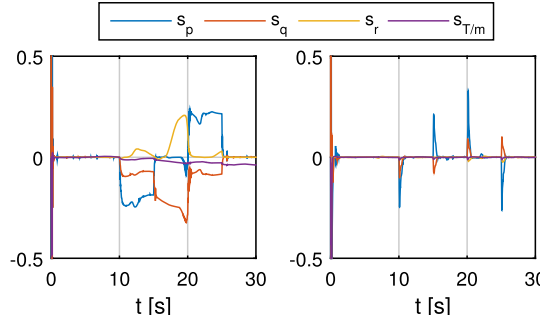


Fig. 22. Attitude and thrust tracking performance using VHG-NTSMC in Scenario 3.

Fig. 21. Responses of  $s_p$ ,  $s_q$ ,  $s_r$ ,  $s_{f T/m}$  using VHG-NTSMC (left) and INTSMC (right) in Scenario 3.

(Fig. 21), a delayed adaption may lead to instability. Furthermore, since  $\|\epsilon_{nt}\|$  is larger than  $\|\epsilon_{int}\|$ , the minimum possible [37,39] control gains for NTSMC are also higher.

By contrast, INTSMC is able to passively resist the perturbations in Scenario 3 with much lower control gains. Gain adjustments or adaptations are not necessary. The resulting control commands are also smoother than that of VHG-NTSMC, as illustrated in Fig. 20. As shown in Fig. 19,  $\epsilon_{int}$  only has spikes in the presence of sudden rotor faults, which is in accordance with analyses in subsection 2.3.  $\|\mathbf{s}_{ro} = [s_p, s_q, s_r, s_{f T/m}]^T\| \leq 0.03$  are reached within 0.8 seconds after faults occur, as presented in Fig. 21.

The attitude and thrust tracking responses of VHG-NTSMC are shown in Fig. 22. It can be seen that although NTSMC using very high control gains can maintain stability, the tracking performance is inevitably reduced. Recall Corollary 1, if  $\epsilon_{nt}$  is bounded, then  $|\epsilon_i| \leq 2\Delta_{nt,s_i} = 2(|\epsilon_{nt,i}|/(k_{2,i} - \eta))^{1/\rho_i}$  in finite time. Therefore, the performance of NTSMC can be improved by increasing  $k_{2,i}$  and reducing  $\rho_i$ . The defects of raising  $k_{2,i}$  have been explained earlier. Reducing  $\rho_i$  however has the risk of inducing chattering, since  $|s_i|^{\rho_i} \text{sign}(s_i) \rightarrow \text{sign}(s_i)$  as  $\rho_i \rightarrow 0$ .

On the contrary, because of the smaller  $\|\epsilon_{int}\|$  (Fig. 19, subsection 2.3), INTSMC has better inner-loop tracking performance without any gain adjustment, which can be seen by comparing Fig. 16 with Fig. 22. The better robustness of INTSMC is also verified in Fig. 23, where  $\|\epsilon_p\| \leq 0.059$  m within 5.9 s, and  $\|\mathbf{s}_p\| \leq 0.068$  m within 2.2 s. Conversely, even though the NTSMC with very high control gains can maintain stability, the performance is significantly degraded by the perturbations.

## 5. Conclusions

This paper proposes incremental nonsingular terminal sliding mode control (INTSMC) for a class of nonlinear uncertain systems. This method adopts a continuous reaching law and a singularity-free nonlinear sliding surface. It is proved that, in the absence of perturbations, INTSMC ensures the system trajectories converge to

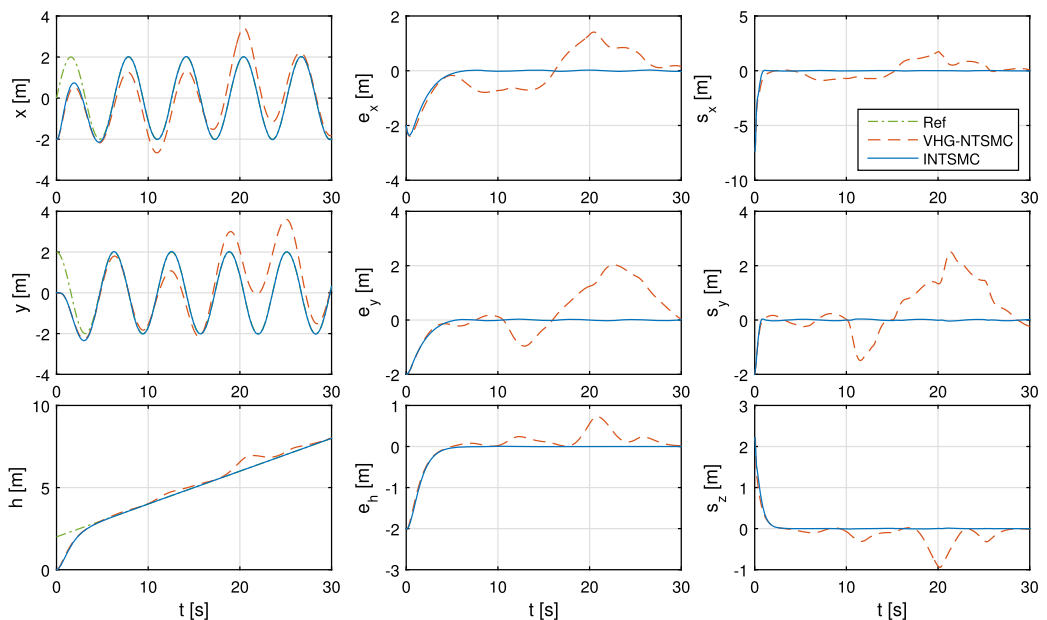


**Fig. 23.** Position responses using very-high-gain (VHG) NTMSC in Scenario 3.

the equilibrium in finite time, while in the presence of bounded perturbations, INTSMC makes the system trajectories converge to a small neighborhood of the equilibrium in finite time. By fully exploiting the sensor measurements, the proposed method can simultaneously reduce model dependency and the remaining uncertainty of the model-based nonsingular terminal sliding mode control (NTSMC) in the literature. The reduced model dependency can simplify the implementation process and alleviate onboard computational load, whereas the reduction of uncertainty decreases the minimum possible sliding mode control gains. These merits are numerically verified by a quadrotor fault-tolerant trajectory control problem. When the same control parameters are used, INTSMC shows better robustness to model uncertainties and external disturbances than NTSMC. Moreover, in the presence of successive actuator faults, the quadrotor using NTSMC crashes because of the unbounded closed-loop perturbation term. Amplifying the switching gains of NTSMC helps to stabilize the impaired quadrotor, but induces severe chattering in the control input. By contrast, the sensor-based INTSMC method can tolerate a wide range of model uncertainties, gusts, and successive sudden actuator faults with much lower switching gains. In addition, the INTSMC input is smooth and free from singularity. Apart from quadrotor trajectory control, the proposed INTSMC method also has the potential to achieve robust and high-precision control of other nonlinear systems such as robotic manipulators and hydraulic rods.

## Declaration of competing interest

There is no conflict of interest.

## References

- [1] J.-J.E. Slotine, W. Li, *Applied Nonlinear Control*, Prentice Hall, Englewood Cliffs, NJ, 1991.
- [2] C. Edwards, S.K. Spurgeon, *Sliding Mode Control: Theory and Applications*, 1st ed., CRC Press, 1998.
- [3] H.K. Khalil, *Nonlinear Systems*, Prentice-Hall, New Jersey, 2002.
- [4] Y. Feng, X. Yu, Z. Man, Non-singular terminal sliding mode control of rigid manipulators, *Automatica* 38 (2002) 2159–2167.
- [5] X. Ai, J. Yu, Fixed-time trajectory tracking for a quadrotor with external disturbances: a flatness-based sliding mode control approach, *Aerosp. Sci. Technol.* 89 (2019) 58–76.
- [6] Y. Tang, Terminal sliding mode control for rigid robots, *Automatica* 34 (1998) 51–56.
- [7] S. Yu, X. Yu, B. Shirinzadeh, Z. Man, Continuous finite-time control for robotic manipulators with terminal sliding mode, *Automatica* 41 (2005) 1957–1964.
- [8] P. Lu, E. van Kampen, C. de Visser, Q.P. Chu, Aircraft fault-tolerant trajectory control using incremental nonlinear dynamic inversion, *Control Eng. Pract.* 57 (2016) 126–141.
- [9] X. Wang, E. van Kampen, Q.P. Chu, R. De Breuker, Flexible aircraft gust load alleviation with incremental nonlinear dynamic inversion, *J. Guid. Control Dyn.* (2019) 1–18.
- [10] X. Wang, E. van Kampen, Q.P. Chu, P. Lu, Incremental sliding-mode fault-tolerant flight control, *J. Guid. Control Dyn.* 42 (2019) 244–259.
- [11] X. Wang, E. van Kampen, Q.P. Chu, P. Lu, Stability analysis for incremental nonlinear dynamic inversion control, *J. Guid. Control Dyn.* (2019).
- [12] X. Wang, S. Sun, E. van Kampen, Q.P. Chu, Quadrotor fault tolerant incremental sliding mode control driven by sliding mode disturbance observers, *Aerosp. Sci. Technol.* 87 (2019) 417–430.
- [13] Y. Feng, X. Yu, F. Han, On nonsingular terminal sliding-mode control of nonlinear systems, *Automatica* 49 (2013) 1715–1722.
- [14] C.E. Hall, Y.B. Shtessel, Sliding mode disturbance observer-based control for a reusable launch vehicle, *J. Guid. Control Dyn.* 29 (2006) 1315–1328.
- [15] Y. Yang, Y. Yan, Attitude regulation for unmanned quadrotors using adaptive fuzzy gain-scheduling sliding mode control, *Aerosp. Sci. Technol.* 54 (2016) 208–217.
- [16] L. Besnard, Y.B. Shtessel, B. Landrum, Quadrotor vehicle control via sliding mode controller driven by sliding mode disturbance observer, *J. Franklin Inst.* 349 (2012) 658–684.
- [17] A.R. Merheb, H. Noura, F. Bateman, Design of passive fault-tolerant controllers of a quadrotor based on sliding mode theory, *Int. J. Appl. Math. Comput. Sci.* 25 (2015) 561–576.
- [18] P.M. Tiwari, S. Janardhanan, M. Un Nabi, Attitude control using higher order sliding mode, *Aerosp. Sci. Technol.* 54 (2016) 108–113.
- [19] M. Defoort, T. Floquet, A. Kokosy, W. Perruquetti, A novel higher order sliding mode control scheme, *Syst. Control Lett.* 58 (2009) 102–108.
- [20] Z. Su, H. Wang, N. Li, Anti-disturbance rapid vibration suppression of the flexible aerial refueling hose, *Mech. Syst. Signal Process.* 104 (2018) 87–105.
- [21] Y. Yu, H. Wang, N. Li, Fault-tolerant control for over-actuated hypersonic reentry vehicle subject to multiple disturbances and actuator faults, *Aerosp. Sci. Technol.* 87 (2019) 230–243.
- [22] Y.B. Shtessel, I.A. Shkolnikov, Aeronautical and space vehicle control in dynamic sliding manifolds, *Int. J. Control.* 76 (2003) 1000–1017.
- [23] Y. Shtessel, J. Buffington, S. Banda, Tailless aircraft flight control using multiple time scale reconfigurable sliding modes, *IEEE Trans. Control Syst. Technol.* 10 (2002) 288–296.
- [24] Y.B. Shtessel, J.M. Buffington, S.S. Banda, Multiple timescale flight control using reconfigurable sliding modes, *J. Guid. Control Dyn.* 22 (1999) 873–883.
- [25] X. Yin, B. Wang, L. Liu, Y. Wang, Disturbance observer-based gain adaptation high-order sliding mode control of hypersonic vehicles, *Aerosp. Sci. Technol.* 89 (2019) 19–30.

- 1 [26] T. Keijzer, G. Looye, Q.P. Chu, E. van Kampen, Design and flight testing of incremental backstepping based control laws with angular accelerometer feedback, in: AIAA Scitech 2019 Forum, January, American Institute of Aeronautics and Astronautics, San Diego, California, 2019, pp. 1–25.
- 2 [27] W. van Ekeren, G. Looye, R.O. Kuchar, Q.P. Chu, E.-J. Van Kampen Design, Implementation and flight-tests of incremental nonlinear flight control methods, in: 2018 AIAA Guidance, Navigation, and Control Conference, January, American Institute of Aeronautics and Astronautics, Kissimmee, Florida, 2018, pp. 1–21.
- 3 [28] E.J.J. Smeur, Q.P. Chu, G.C.H.E. de Croon, Adaptive incremental nonlinear dynamic inversion for attitude control of micro air vehicles, *J. Guid. Control Dyn.* 39 (2016) 450–461.
- 4 [29] S. Sun, L. Sijbers, X. Wang, C. de Visser, High-speed flight of quadrotor despite loss of single rotor, *IEEE Robot. Autom. Lett.* 3 (2018) 3201–3207.
- 5 [30] B. Etkin, *Dynamics of Atmospheric Flight*, Dover Publications, Toronto, 2005.
- 6 [31] S. Sun, C.C. de Visser, Q. Chu, Quadrotor gray-box model identification from high-speed flight data, *J. Aircr.* 56 (2018) 1–17.
- 7 [32] E.J.J. Smeur, G.C.H.E. de Croon, Q.P. Chu, Cascaded incremental nonlinear dynamic inversion for MAV disturbance rejection, *Control Eng. Pract.* 73 (2018) 79–90.
- 8 [33] A. Modirrousta, M. Khodabandeh, A novel nonlinear hybrid controller design for an uncertain quadrotor with disturbances, *Aerosp. Sci. Technol.* 45 (2015) 294–308.
- 9 [34] Z. Jia, J. Yu, Y. Mei, Y. Chen, Y. Shen, X. Ai, Integral backstepping sliding mode control for quadrotor helicopter under external uncertain disturbances, *Aerosp. Sci. Technol.* 68 (2017) 299–307.
- 10 [35] X. Wang, E. van Kampen, Q.P. Chu, Gust load alleviation and ride quality improvement with incremental nonlinear dynamic inversion, in: AIAA Atmospheric Flight Mechanics Conference, American Institute of Aeronautics and Astronautics, Grapevine, Texas, 2017, pp. 1–21.
- 11 [36] Z. Song, K. Sun, Adaptive fault tolerant control for a small coaxial rotor unmanned aerial vehicles with partial loss of actuator effectiveness, *Aerosp. Sci. Technol.* 88 (2019) 362–379.
- 12 [37] C. Edwards, Y.B. Shtessel, Adaptive continuous higher order sliding mode control, *Automatica* 65 (2016) 183–190.
- 13 [38] C. Edwards, Y. Shtessel, Adaptive dual-layer super-twisting control and observation, *Int. J. Control.* 89 (2016) 1759–1766.
- 14 [39] V.I. Utkin, A.S. Poznyak, Adaptive sliding mode control with application to super-twist algorithm: equivalent control method, *Automatica* 49 (2013) 39–47.

67  
68  
69  
70  
71  
72  
73  
74  
75  
76  
77  
78  
79  
80  
81  
82  
83  
84  
85  
86  
87  
88  
89  
90  
91  
92  
93  
94  
95  
96  
97  
98  
99  
100  
101  
102  
103  
104  
105  
106  
107  
108  
109  
110  
111  
112  
113  
114  
115  
116  
117  
118  
119  
120  
121  
122  
123  
124  
125  
126  
127  
128  
129  
130  
131  
132